Hunting for hypercharge anapole dark matter in all spin scenarios

Seong Youl Choi,[1,*] Jaehoon Jeong,[2,†] Dong Woo Kang,[1,‡] and Seodong Shin[1,§]

[1]*Laboratory for Symmetry and Structure of the Universe, Department of Physics, Jeonbuk National University, Jeonju, Jeonbuk 54896, Korea*

[2]*School of Physics, Korea Institute for Advanced Study, Seoul 02455, Korea*

(Received 19 January 2024; accepted 5 April 2024; published 1 May 2024)

We conduct a combined analysis to investigate dark matter (DM) with hypercharge anapole moments, focusing on scenarios where Majorana DM particles with spin $1/2$, 1, $3/2$, and 2 interact exclusively with Standard Model particles through $\mathrm{U}(1)_Y$ hypercharge anapole terms for the first time. For completeness, we construct general effective U(1) gauge-invariant three-point vertices. These enable the generation of hypercharge gauge-invariant interaction vertices for both a virtual photon γ and a virtual Z boson with two identical massive Majorana particles of any nonzero spin s, after the spontaneous breaking of electroweak gauge symmetry. For complementarity, we adopt effective operators tailored to each dark matter spin allowing crossing symmetry. We calculate the relic abundance, analyze current constraints and future sensitivities from dark matter direct detection and collider experiments, and apply the conceptual naive perturbativity bound. Our estimations based on a generalized vertex calculation demonstrate that the scenario with a higher-spin DM is more stringently constrained than a lower-spin DM, primarily due to the reduced annihilation cross section and/or the enhanced rate of LHC monojet events. As a remarkable outcome, the spin-2 anapole DM scenario is almost entirely excluded, while the high-luminosity LHC exhibits high sensitivities in probing spin-1 and -$3/2$ scenarios, except for a tiny parameter range of DM mass around 1 TeV. A significant portion of the remaining parameter space in the spin-$1/2$ DM scenario can be explored through upcoming Xenon experiments, with more than 20 ton-yr exposure equivalent to approximately 5 years of running the XENONnT experiment.

DOI: 10.1103/PhysRevD.109.096001

I. INTRODUCTION

The nature of dark matter (DM) remains one of the greatest puzzles in particle physics and cosmology, accounting for approximately a quarter of the total energy content in the Universe. Exploring the nongravitational interactions of DM with Standard Model (SM) particles offers a direct path to uncovering new structures and symmetries. This exploration can be pursued through three distinct experimental approaches: direct detection, indirect detection, and collider experiments. These three different types of experiments can be complementary to one another, and hence it is extremely helpful to combine the results and apply them to a single effective operator for DM/SM interactions. This is a reasonable and widely applicable approach in scenarios where the corresponding effective field theory (EFT) is valid [1–4].

Certainly, for a proper EFT description, it is required that the energy scale of all processes under consideration be well below the masses of the mediating particles, and that their interactions respect the established low-energy (global and/or gauge) symmetries of the SM [5–8]. As the TeV energy scale, which is higher than the electroweak scale, is currently being probed and the SM with its $\mathrm{SU}(3)_C \times \mathrm{SU}(2)_L \times \mathrm{U}(1)_Y$ gauge symmetry has been firmly established, particularly with the discovery of the Higgs boson [9,10], it is appropriate to maintain both the hypercharge $\mathrm{U}(1)_Y$ symmetry and the other non-Abelian gauge symmetries, $\mathrm{SU}(3)_C$ and $\mathrm{SU}(2)_L$. For instance, the importance of considering the hypercharge $\mathrm{U}(1)_Y$ rather than the electromagnetic $\mathrm{U}(1)_{\mathrm{EM}}$ as a valid U(1) gauge symmetry has been clearly and persuasively demonstrated from various physics perspectives in recent work [11].

The nongravitational interaction between DM and SM particles through an electromagnetic (EM) form factor, for DM with nonzero spin, is realized through a higher-dimensional operator. Consequently, this provides an interesting test bed for the EFT approach in DM studies.

*sychoi@jbnu.ac.kr
†jeong229@kias.re.kr
‡dongwookang@jbnu.ac.kr
§sshin@jbnu.ac.kr

TABLE I. Comparison between our current research and various previous studies on EM anapole DM and hypercharge anapole DM conducted through three main experiments: relic abundance analysis, searches at the LHC, and/or direct detection experiments. The works are referenced with corresponding citation numbers provided in the references. In the case of spin-1 EM anapole DM, each cross mark (✗) denotes that the relic abundance and LHC search aspects have not been explored to date. On the other hand, the check mark (✓) signifies the comprehensive quantitative investigation of all the clarified experimental aspects in the spin-1, -3/2, and -2 cases in addition to the spin-1/2 case, undertaken in our current work.

	EM anapole DM		Hypercharge anapole DM			
Scenario (Spin)	1/2	1	1/2	1	3/2	2
Relic abundance	[62] [66] [70]	✗	[11]	This work ✓		
LHC search	[64] [67] [69]	✗	[11]			
Direct detection	[62] [65] [67] [68] [70]	[71] [72]	[11]			

Additionally, the EM form factor induces unexpected (and suppressed) EM interactions of DM with SM particles, without the DM being directly charged. The phenomenological effects of such interactions were first discussed in Ref. [12].

In this paper, we adopt an EFT approach for scenarios involving *CPT* self-conjugate Majorana DM with spin 1/2 to 2, where interactions with SM particles are exclusively mediated through $U(1)_Y$ hypercharge anapole terms. For neutralino DM in supersymmetric models, which has been the most preferred and theoretically well-motivated DM candidate over the past decades, the corresponding anapole term is the only allowed U(1) form factor, and hence it is worthwhile to study in detail [13–15]. The first Kaluza-Klein excitation of the hypercharge gauge boson is a typical candidate for a spin-1 Majorana particle interacting with the SM particles through hypercharge anapole terms. The scenario involving spin-1 DM particles has been investigated in various works [16–30]. The spin-3/2 DM has been well studied as a gravitino in supergravity and also in various effective theories [31–45]. The massive graviton, expected to exist in extra-dimensional models and bigravity theories, has been widely discussed as a spin-2 DM candidate [43,46–61].

Previously, several aspects of EM anapole DM interaction terms have been studied in the context of relic abundance measurements as well as in searches at direct detection, indirect detection, and collider experiments for the spin-1/2 case [62–70] and the spin-1 case [71,72]. A comprehensive analysis of the $U(1)_Y$ anapole DM scenario with a spin-1/2 Majorana particle was recently conducted [11]. On the contrary, the analysis for the spin-1 case was restricted so far to the EM anapole DM scenario, as the focus was only on the direct DM detection capability. In this context, it is worthwhile to perform a generic analysis accommodating and characterizing the hypercharge anapole DM particle of any nonzero spin with combined experimental probes all together.

In our general analysis, we construct effective $U(1)_Y$ gauge-invariant three-point vertices of a hypercharge gauge boson B and two identical on-shell Majorana particles with any nonzero spin.[1] These vertices accommodate an arbitrary spin s and nonzero mass m, generating interaction vertices with not only a virtual photon γ but also a virtual gauge boson Z after electroweak symmetry breaking (EWSB). A concise overview of the distinction between our analysis targets and those of other studies is shown in Table I.

Having outlined the general three-point vertices, our in-depth numerical analysis is specifically targeted toward four scenarios where the DM particle spin is set to be 1/2, 1, 3/2, and 2, while qualitatively exploring the implications for the scenarios with its spin larger than 2. We incorporate the relic abundance value determined by the Planck Collaboration [74], the up-to-date result from the DM direct detection experiment XENONnT with approximately 1.1 ton-yr exposure [75], and the LHC experiments with the integrated luminosity of 139 fb^{-1} [76–78] as well as the so-called naive perturbativity bound (NPB) making our EFT approach valid.[2] In addition, we estimate the projected sensitivities of the high-luminosity LHC (HL-LHC) experiment with the full run of 3 ab^{-1} integrated luminosity [79] and those of the future XENONnT with the 20 ton-yr exposure.

This paper is organized as follows. In Sec. II, we derive the general effective hypercharge gauge-invariant three-point vertices. These generate interaction vertices for a virtual photon γ and a massive gauge boson Z with two identical on-shell particles of any nonzero spin s and mass m, following EWSB. The derivation is based on an efficient and systematic algorithm for constructing the covariant effective vertex for three particles of any spin and mass [80–82]. In Sec. III, we calculate the annihilation cross sections of two Majorana particles into kinematically

[1]For clarity, the term "Majorana particle" is conventionally used to represent a spin-1/2 self-conjugate particle; however, we will generalize it to include self-conjugate particles of any spin without loss of generality, as done in Ref. [73].

[2]Conceptually, there could also be unitarity bounds on the couplings for each annihilation mode, but these are quantitatively much weaker than the naive perturbativity limits.

allowed pairs of SM particles. We then determine the constraints on the effective coupling strengths for the spin-1/2, 1, 3/2, and 2 cases from the observed DM relic abundance. Section IV is devoted to determining constraints on the coupling strengths from recent LHC and upcoming HL-LHC experiments [76,79]. We particularly focus on how these constraints depend on the spin of the anapole DM Majorana particle. In Sec. V, we explore constraints from the up-to-date results of the DM direct detection experiment XENONnT [75] and the projected sensitivities from its highly enhanced exposure and study the implications for the coupling strengths. Based on all the experimental constraints and an additional theoretical constraint from the naive perturbativity bound, we present an overall combined picture of the current constraints and sensitivities in Sec. VI. This comprehensive analysis places special emphasis on systematically delineating the distinct characteristics that vary depending on the spin values. We summarize the key points of our results and conclude in Sec. VII. Furthermore, Appendix A provides a concise and systematic algorithmic description for constructing all the general three-point anapole vertices efficiently, and Appendix B provides a detailed explanation of the numerical calculation strategy employed to determine the DM relic abundance.

II. ANAPOLE VERTICES FOR TWO MAJORANA PARTICLES OF ANY SPIN

In this section, we present an efficient and systematic algorithm for constructing covariant three-point anapole vertices for two identical Majorana particles of any spin. This algorithm allows us to perform a complete and systematic characterization of all the spin values of the hypercharge anapole DM. Subsequently, we delve deeper into the specific case of covariant vertices, focusing on the spin-1/2, -1, -3/2, and -2 scenarios. This detailed analysis encompasses both analytic and numerical investigations to provide comprehensive insights and findings.

A. Aanapole three-point vertices of Majorana particles of any spin

A Majorana particle, by definition, is a *CPT* self-conjugate particle, which means it remains unchanged under the combined operations of charge conjugation (C), parity reversal (P), and time reversal (T). These particles do not possess any static charge or multipole moments, as all the terms in their interaction Hamiltonian are *CPT* odd.

The only permissible U(1) gauge-invariant interaction vertices between a U(1) gauge boson and two identical massive Majorana particles of nonzero spin are known as anapole-type moments [73]. It is worth noting that no massless *CPT* self-conjugate Majorana particle can have any U(1) gauge-invariant couplings unless its spin is 1/2.

The effective anapole three-point $\chi\chi B$ vertex of two identical massive Majorana particles χ of any spin and a U(1) gauge boson B is in general given by the gauge-invariant Lagrangian

$$\mathcal{L}_{\text{anapole}} = \mathcal{J}_\mu \partial_\nu B^{\mu\nu}, \tag{2.1}$$

with the 4-vector current $\mathcal{J}_\mu$ comprising two Majorana-particle fields and the field-strength tensor $B^{\mu\nu} = \partial^\mu B^\nu - \partial^\nu B^\mu$ of the U(1) gauge boson B.

Equation (2.1) enables us to construct the effective conserved current for the annihilation of two Majorana particles into a virtual vector boson depicted in Fig. 1. Explicitly, the current can be cast into the form

$$V_\mu(p,q) = p^2 J_\mu(p,q) - p \cdot J(p,q) p_\mu, \tag{2.2}$$

with $p = k_1 + k_2$ and $q = k_1 - k_2$ in terms of the incoming Majorana-particle momenta, k_1 and k_2, where the vector current J_μ is nothing but the momentum-representation version of the position-representation current $\mathcal{J}_\mu$ in Eq. (2.1). Note that the vector current V_μ automatically satisfies the U(1) gauge invariance condition $p^\mu V_\mu = 0$. In the covariant formulation, the vector current V_μ can be written as the products between the wave tensors $\chi_s(k_1)$ and $\chi_s(k_2)$ of two Majorana particles and a covariant three-point vertex Γ,

$$V_\mu(p,q) = \bar{\chi}_s^\beta(k_2)\Gamma_{\alpha,\beta;\mu}(p,q)\chi_s^\alpha(k_1), \tag{2.3}$$

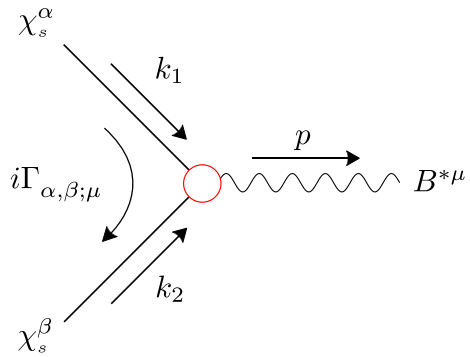

FIG. 1. A diagram for the annihilation of two identical Majorana particles χ_s into an off-shell hypercharge gauge boson B^*. The combined momenta $p = k_1 + k_2$ and $q = k_1 - k_2$ are constructed by the combinations of incoming momenta $k_{1,2}$ of two Majorana particles. The $k_{1,2}$-dependent χ_s^α and χ_s^β are the wave functions of two identical Majorana particles with the particle symbol denoted by χ in the main text. The indices, α and β, stand collectively for the 4-vector indices, $\alpha = \alpha_1 \cdots \alpha_n$ and $\beta = \beta_1 \cdots \beta_n$, with $n = s - 1/2$ or $n = s$ for a half-integer or integer spin-s Majorana particle. The curved arrow is for an arbitrary chosen fermion-number flow direction whose meaning is described in detail in Refs. [83,84].

with respect to the arbitrarily chosen fermion-number-flow arrow shown in Fig. 1, where the indices, α and β, stand collectively for the 4-vector indices, $\alpha = \alpha_1 \cdots \alpha_n$ and $\beta = \beta_1 \cdots \beta_n$, with $n = s - 1/2$ or $n = s$ for a half-integer or integer spin-s Majorana particle. All the details about the wave tensors [85–90] and the general covariant vertices are included collectively in Appendix A.

As two identical Majorana particles annihilate into a virtual gauge boson B^*, the covariant three-point vertex must satisfy the so-called identical-particle (IP) condition, Eq. (A23) or (A24), in the fermionic or bosonic case, respectively, as described in detail in Appendix A. By employing the general covariant three-point vertices and imposing the IP relation, the anapole three-point vertices can be cast into a compact square-bracket operator form,

$$[\Gamma_F] = \left(\frac{p^2}{\Lambda^2}\right)[A]\sum_{\tau=0}^{n}\left(\frac{p^2}{\Lambda^2}\right)^{\tau} f_\tau^-[g]^{n-\tau}[S^0]^\tau + \left(\frac{p^2\sqrt{p^2}}{\Lambda^3}\right)[V]\sum_{\tau=1}^{n}\left(\frac{p^2}{\Lambda^2}\right)^{\tau-1} \times f_\tau^+[g]^{n-\tau}[S^0]^{\tau-1} \quad \text{for fermions,} \tag{2.4}$$

$$[\Gamma_B] = \sqrt{p^2}\left(\frac{p^2}{\Lambda^2}\right)\sum_{\tau=1}^{n}\left(\frac{p^2}{\Lambda^2}\right)^{\tau-1} \times (b_\tau^-[V^-] + b_\tau^+[V^+])[g]^{n-\tau}[S^0]^{\tau-1} \quad \text{for bosons,} \tag{2.5}$$

in terms of $2s$ independent f and b couplings for the spin-s Majorana fermion with $s = n + 1/2$ and boson with $s = n$, respectively. The cutoff scale Λ is set forth explicitly to indicate that the effective covariant vertex originates from a higher-dimensional operator term in the given effective Lagrangian or Hamiltonian. Here, the square-bracket notations are introduced for denoting the product of the basic helicity-related operators as well as two derived operators in a compact form with all the 4-vector and spinor index symbols hidden.

First, the two square-bracket operators, $[A]$ and $[V]$, in Eq. (2.4) denote an orthogonal axial-vector and vector currents, of which the explicit forms are given by

$$[A] \to A_\mu = \gamma_{\perp\mu}\gamma_5, \tag{2.6}$$

$$[V] \to V_{\alpha\beta;\mu} = \hat{p}_\alpha g_{\perp\beta\mu} + \hat{p}_\beta g_{\perp\alpha\mu}, \tag{2.7}$$

with an orthogonal gamma matrix $\gamma_{\perp\mu} = g_{\perp\mu\nu}\gamma^\nu$ and an orthogonal metric tensor $g_{\perp\mu\nu} = g_{\mu\nu} - \hat{p}_\mu\hat{p}_\nu + \hat{q}_\mu\hat{q}_\nu$ involving two normalized momenta, $\hat{p} = p/\sqrt{p^2}$ and $\hat{q} = q/\sqrt{-q^2}$. Second, due to the totally symmetric property of the wave tensors [85–90] over all the 4-vector indices, the nth power products of the metric tensor g and the basic scalar operator S^0 can be given in a compact square-bracket form,

$$[g]^n \to g_{\alpha_1\beta_1}\cdots g_{\alpha_n\beta_n}, \tag{2.8}$$

$$[S^0]^n \to S^0_{\alpha_1\beta_1}\cdots S^0_{\alpha_n\beta_n}, \tag{2.9}$$

where the basic scalar operator S^0 is defined by

$$S^0_{\alpha\beta} = \hat{p}_\alpha\hat{p}_\beta, \tag{2.10}$$

of which the repeated appearance at the vertices increases the dimensions of the corresponding Lagrangians gradually. It is compensated by introducing the proper power of the cutoff scale Λ along with the operator as shown in Eqs. (2.4) and (2.5). Third, the other two derived basic vector operators $[V^\pm]$ are defined by

$$[V^\pm] \to V^\pm_{\alpha\beta;\mu} = \hat{p}_\beta S^\pm_{\alpha\mu} + \hat{p}_\alpha S^\mp_{\beta\mu}, \tag{2.11}$$

in terms of the normalized momentum $\hat{p}$ and the basic scalar operators $S^\pm$ of which the explicit expression is

$$S^\pm_{\alpha\beta} = \frac{1}{2}[g_{\perp\alpha\beta} \pm i\langle\alpha\beta\hat{p}\,\hat{q}\rangle], \tag{2.12}$$

with the angle-bracket notation $\langle\alpha\beta\hat{p}\,\hat{q}\rangle = \varepsilon_{\alpha\beta\rho\sigma}\hat{p}^\rho\hat{q}^\sigma$ of a product between an antisymmetric Levi-Civita tensor and two normalized momenta $\hat{p}$ and $\hat{q}$.

B. Effective three-point anapole vertices for the spin of 1/2, 1, 3/2, and 2

Following the systematic derivation procedure for constructing the general anapole vertices and using the general properties of wave tensors described in Appendix A, we can recast the covariant three-point anapole vertices extracted from the general forms in Eqs. (2.4) and (2.5) effectively into the following form as

$$\Gamma^{[1/2]}_\mu \overset{\text{eff}}{=} \frac{p^2}{\Lambda^2}a_{1/2}\gamma_{\perp\mu}\gamma_5, \tag{2.13}$$

$$\Gamma^{[1]}_{\alpha,\beta;\mu} \overset{\text{eff}}{=} \frac{ip^2}{\Lambda^2}[a_1\langle\alpha\beta\mu q\rangle_\perp - b_1(p_\alpha g_{\perp\beta\mu} + p_\beta g_{\perp\alpha\mu})], \tag{2.14}$$

in terms of a single coupling $a_{1/2}$ in the spin-1/2 case and two independent couplings, a_1 and b_1, in the spin-1 case with an orthogonal antisymmetric tensor $\langle\alpha\beta\mu q\rangle_\perp = g_{\perp\mu\nu}\epsilon_{\alpha\beta}{}^{\nu\sigma}q_\sigma$, and

$$\Gamma^{[3/2]}_{\alpha,\beta;\mu} \overset{\text{eff}}{=} \frac{p^2}{\Lambda^2}a_{3/2}\gamma_{\perp\mu}\gamma_5 g_{\alpha\beta}, \tag{2.15}$$

$$\Gamma^{[2]}_{\alpha_1\alpha_2,\beta_1\beta_2;\mu} \overset{\text{eff}}{=} \frac{ip^2}{\Lambda^2}[a_2\langle\alpha_1\beta_1\mu q\rangle_\perp - b_2(p_{\alpha_1}g_{\perp\beta_1\mu} + p_{\beta_1}g_{\perp\alpha_1\mu})]g_{\alpha_2\beta_2}, \tag{2.16}$$

in terms of a single coupling $a_{3/2}$ in the spin-3/2 case and two independent couplings, a_2 and b_2, in the spin-2 case up to the leading order in $1/\Lambda^2$. All the couplings are in general complex, and the a_i terms are parity odd, while the b_j terms are parity even where $i = 1/2, 1, 3/2, 2$ and $j = 1, 2$. Although our numerical analysis is confined up to spin 2, a simple extrapolation suggests that a single coupling exists in any half-integer spin scenario, while in the case of nonzero integer spin, there are two distinct and independent couplings at the leading order of $1/\Lambda^2$, as evident with Eqs. (2.4) and (2.5).

The effective U(1) gauge-invariant spin-1/2 and spin-1 anapole Lagrangians corresponding to the vertices in Eqs. (2.13) and (2.14) can be reconstructed by replacing each momentum with its corresponding derivative as

$$\mathcal{L}_{1/2} = \frac{a_{1/2}}{2\Lambda^2}\bar{\chi}_{\frac{1}{2}}\gamma^\mu\gamma_5\chi_{\frac{1}{2}}\partial_\nu B^{\mu\nu}, \tag{2.17}$$

$$\mathcal{L}_1 = \left[\frac{a_1}{2\Lambda^2}\epsilon_{\alpha\beta\mu\rho}[\chi_1^\alpha(\partial^\rho\chi_1^\beta) - (\partial^\rho\chi_1^\alpha)\chi_1^\beta] + \frac{b_1}{2\Lambda^2}\partial^\rho(\chi_{1\rho}\chi_{1\mu} + \chi_{1\mu}\chi_{1\rho})\right]\partial_\nu B^{\mu\nu}, \tag{2.18}$$

in terms of the spin-1/2 and spin-1 Majorana fields, $\chi_{\frac{1}{2}}$ and $\chi_{1\mu}$, respectively. Likewise, the U(1) gauge-invariant spin-3/2 and spin-2 anapole Lagrangians corresponding to the vertices in Eqs. (2.15) and (2.16) are given as

$$\mathcal{L}_{3/2} = \frac{a_{3/2}}{2\Lambda^2}\bar{\chi}_{\frac{3}{2}\rho}\gamma^\mu\gamma_5\chi_{\frac{3}{2}}^\rho\partial_\nu B^{\mu\nu}, \tag{2.19}$$

$$\mathcal{L}_2 = \left[\frac{a_2}{2\Lambda^2}\epsilon_{\alpha\beta\mu\rho}[\chi_2^{\alpha\sigma}(\partial^\rho\chi_{2\sigma}^\beta) - (\partial^\rho\chi_2^{\alpha\sigma})\chi_{2\sigma}^\beta] + \frac{b_2}{2\Lambda^2}\partial^\rho(\chi_{2\rho}^\sigma\chi_{2\mu\sigma} + \chi_{2\mu}^\sigma\chi_{2\rho\sigma})\right]\partial_\nu B^{\mu\nu}, \tag{2.20}$$

in terms of the spin-3/2 and spin-2 Majorana fields, $\chi_{\frac{3}{2}\mu}$ and $\chi_{2\mu\nu}$, respectively.

In the following, we specify the U(1) gauge boson to be the hypercharge $\mathrm{U}(1)_Y$ gauge boson B in the SM. The hypercharge gauge field B_μ is decomposed into a photon field A_μ and a Z-boson field Z_μ as $B_\mu = c_W A_\mu - s_W Z_\mu$ with $c_W = \cos\theta_W$ and $s_W = \sin\theta_W$ of the weak mixing angle θ_W after the firmly established EWSB. Furthermore, for simplicity and without loss of generality, we omit the spin index s of the Majorana particle χ_s in the following discussion, as it applies universally across all spin cases.

III. DM RELIC ABUNDANCE

In this section, we calculate the relic abundance of our anapole DM of each spin from the thermal freeze-out mechanism. The overabundant region beyond the observed relic abundance [74] is simply considered to be excluded without introducing late time reduction possibilities. The corresponding areas are shown in the two-dimensional planes of mass of dark matter and the couplings a_i, b_j normalized by the cutoff scale squared Λ^2.

The self-conjugate hypercharge anapole DM particles can annihilate into the SM particles via the s-channel photon γ and Z-boson exchanges. If kinematically allowed, the DM particles annihilate mainly via the processes $\chi\chi \to f\bar{f}$, W^-W^+, and/or ZH, where f is a SM quark $q = u, d, s, c, b, t$ or lepton $\ell = e, \mu, \tau, \nu_e, \nu_\mu, \nu_\tau$, as depicted in Fig. 2. The relic abundance of χ can be determined through the freeze-out of the annihilation processes in the figure. As noted previously in Ref. [73], every annihilation cross section is completely factored into a simple product of two independent parts, of which one corresponds to the DM annihilation into a virtual gauge boson and the other of which corresponds to the sequential decay of the virtual gauge boson into a pair of SM particles.[3] Explicitly, the total cross section of each annihilation mode can be written in the compact form

$$\sigma_{1/2} = \frac{|a_{1/2}|^2}{4\Lambda^4}\beta_\chi s\mathcal{P}_{\mathrm{SM}}, \tag{3.1}$$

$$\sigma_1 = \frac{|a_1|^2\beta_\chi^2 + |b_1|^2}{9\Lambda^4}\left(\frac{s}{4m_\chi^2}\right)\beta_\chi s\mathcal{P}_{\mathrm{SM}} \tag{3.2}$$

for the spin-1/2 and spin-1 Majorana particles, respectively, and

$$\sigma_{3/2} = \frac{|a_{3/2}|^2}{72\Lambda^4}(5 - 2\beta_\chi^2 + 5\beta_\chi^4)\left(\frac{s}{4m_\chi^2}\right)^2\beta_\chi s\mathcal{P}_{\mathrm{SM}}, \tag{3.3}$$

$$\sigma_2 = \frac{1}{300\Lambda^4}[|a_2|^2\beta_\chi^2(7 - 6\beta_\chi^2 + 15\beta_\chi^4) + |b_2|^2(15 - 6\beta_\chi^2 + 7\beta_\chi^4)]\left(\frac{s}{4m_\chi^2}\right)^3\beta_\chi s\mathcal{P}_{\mathrm{SM}} \tag{3.4}$$

for the spin-3/2 and spin-2 Majorana particles, respectively, with the collision energy $\sqrt{s}$ and the speed of χ, $\beta_\chi = \sqrt{1 - 4m_\chi^2/s}$ in the c.m. frame of two χ particles. Here, the dimensionless SM pair-production term $\mathcal{P}_{\mathrm{SM}} = \sum_f \mathcal{P}_{f\bar{f}} + \mathcal{P}_{WW} + \mathcal{P}_{ZH}$ is the sum of all the kinematically allowed production terms,

[3]The angular distribution of each annihilation mode is uniquely determined independently of the DM particle spin. This characteristic spin-independent angular distribution was demonstrated explicitly in the scattering process $e^-e^+ \to \gamma^* \to \chi\chi$ via a photon exchange in Ref. [73].

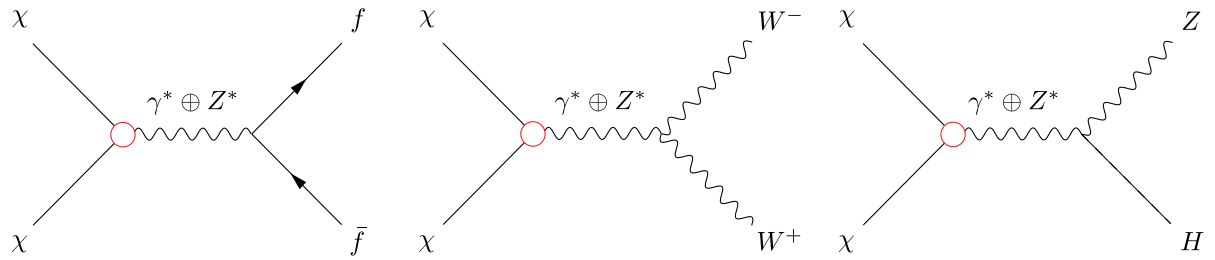

FIG. 2. Feynman diagrams for the dominant annihilation processes of two identical Majorana particles into a pair of SM particles, $\chi\chi \to f\bar{f}$ (left), W^-W^+ (middle), and ZH (right) where f is a SM quark $q = u, d, s, c, b, t$ or lepton $\ell = e, \mu, \tau, \nu_e, \nu_\mu, \nu_\tau$. Here, χ denotes the self-annihilating Majorana DM particle. The red open circle in each diagram indicates the effective three-point anapole vertex. The notation $\gamma^* \oplus Z^*$ stands for the combined s-channel γ and Z exchanges.

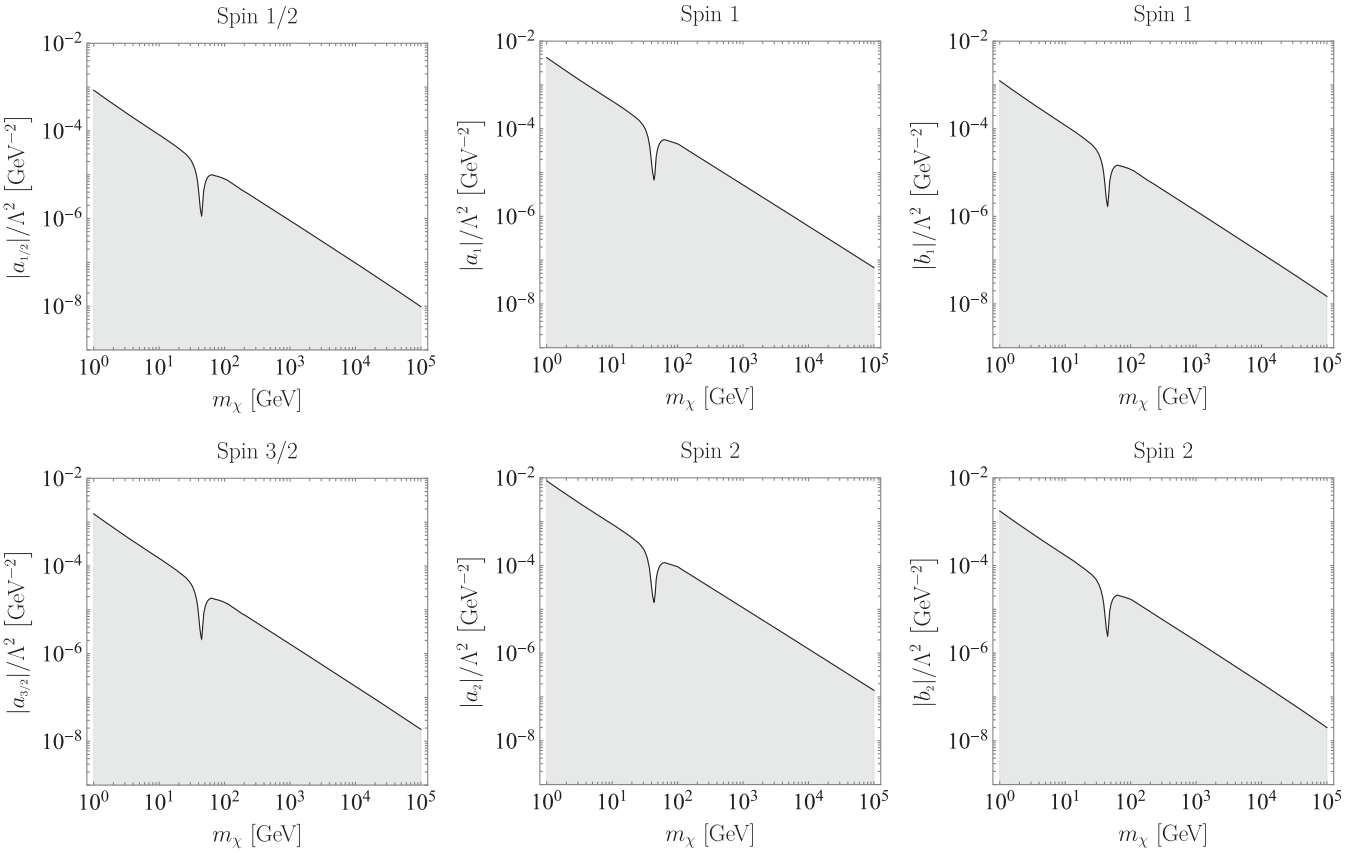

FIG. 3. Exclusion limits on the effective anapole couplings versus the DM mass from the observed DM relic abundance. The top (bottom) left panel shows the constraint on the normalized coupling $|a_{1/2}|/\Lambda^2$ ($|a_{3/2}|/\Lambda^2$) in the spin-1/2 (spin-3/2) case. The top (bottom) middle panel shows the constraint on the normalized coupling $|a_1|/\Lambda^2$ ($|a_2|/\Lambda^2$), and the top (bottom) right panel shows the constraint on the normalized couplings $|b_1|/\Lambda^2$ ($|b_2|/\Lambda^2$) in the spin-1 (spin-2) case. In each plot, the gray-shaded region is excluded by making DM overabundant and bounded by the relic density line (black solid).

$$\mathcal{P}_{f\bar{f}} = \frac{e^2}{12\pi c_W^2}\beta_f \Pi_Z(s)[(3-\beta_f^2)\bar{V}_f^2 + 2\beta_f^2 A_f^2]\theta(\sqrt{s}-2m_f), \tag{3.5}$$

$$\mathcal{P}_{WW} = \frac{e^2}{96\pi c_W^2}(1+\Gamma_Z^2/m_Z^2)\beta_W^3 \Pi_Z(s) \times (1+20m_W^2/s+12m_W^4/s^2)\theta(\sqrt{s}-2m_W), \tag{3.6}$$

$$\mathcal{P}_{ZH} = \frac{e^2}{96\pi c_W^2}\bar{\beta}_{ZH}\Pi_Z(s)(1+8m_Z^2/s)\theta(\sqrt{s}-m_Z-m_H), \tag{3.7}$$

with $\beta_{f,W} = \sqrt{1-4m_{f,W}^2/s}$ and $\bar{\beta}_{ZH} = \sqrt{[1-(m_Z+m_H)^2/s][1-(m_Z-m_H)^2/s]}$. Here, for the

sake of notation, the normalized propagator factor $\Pi_Z(s)$ and an effective SM vector coupling squared $\bar{V}_f^2$ are introduced as

$$\Pi_Z(s) = \frac{s^2}{(s-m_Z^2)^2 + m_Z^2\Gamma_Z^2}, \tag{3.8}$$

$$\bar{V}_f^2(s) = V_f^2 - 2c_W^2 Q_f V_f\left(1 - \frac{m_Z^2}{s}\right) + c_W^4 \frac{Q_f^2}{\Pi_Z(s)}, \tag{3.9}$$

in terms of the SM vector and axial-vector couplings, $V_f = I_f^3/2 - Q_f s_W^2$ and $A_f = -I_f^3/2$, of the Z boson to a SM fermion pair $f\bar{f}$ with the isospin component I_f^3 and electric charge Q_f of the fermion f. We emphasize again that the SM production terms are independent of the DM particle spin and its couplings to the photon and Z boson. Consequently, the information on the characteristics of the anapole DM particle is encoded exclusively in the DM annihilation into a virtual gauge boson.

By calculating the DM relic abundance using the methodology described in detail in Appendix B, we can derive exclusion limits on the effective anapole couplings versus the DM mass. These limits are based on the observed relic abundance of $\Omega_\chi h^2 \approx 0.12$, as illustrated in Fig. 3. Each plot features a gray shaded region that represents an overabundance of DM and is bounded by the relic density line (black solid) obtained from the freeze-out mechanism. The top (bottom) left panel is for the normalized coupling $|a_{1/2}|/\Lambda^2$ ($|a_{3/2}|/\Lambda^2$) versus the DM mass m_χ in the spin-1/2 (spin-3/2) case, the top (bottom) middle panel is for the normalized coupling $|a_1|/\Lambda^2$ ($|a_2|/\Lambda^2$) versus the DM mass m_χ in the spin-1 (spin-2) case, and the top (bottom) right panel is for the normalized coupling $|b_1|/\Lambda^2$ ($|b_2|/\Lambda^2$) versus the DM mass m_χ in the spin-1 (spin-2) case. The single-power dependence of the fermionic annihilation cross sections on the χ speed β_χ in Eq. (3.1) implies that each DM annihilation is a p-wave dominant process in the fermionic cases. On the other hand, the bosonic DM annihilation cross sections include the d-wave dominant terms proportional to the coupling a_1 or a_2 in addition to the p-wave dominant ones with the coupling b_1 or b_2. Hence, the cross sections can be further suppressed by β_χ^4 once a UV model expects b_1 or b_2 is negligible, as can be clearly seen in the right panels of Fig. 3. Note that the p-wave dominant terms $|b_{1,2}|/\Lambda^2$ are more strongly constrained than the $|a_{1/2,3/2}|/\Lambda^2$ from the observed relic abundance due to the reduced spin-averaged and polarization-weighted factors as shown in Eqs. (3.1) and (3.2). Typically, due to the smaller spin averaged factors in the annihilation cross sections, higher-spin DM particles face more stringent constraints compared to the lower-spin cases with the same order of suppression factor β_χ.

IV. LHC SEARCHES

In this section, we derive the exclusion limits on the couplings for the hypercharge anapole DM particle from its searches at the LHC experiment with the projected sensitivities on the couplings from the upcoming HL-LHC experiment [77,78,91,92]. Although there are possibly various production channels at the LHC, we consider the most dominant production processes for the hypercharge anapole DM particle in our analytic analysis.

It was shown in a previous work [69] that the EM anapole DM particles in the $U(1)_{EM}$ gauge-invariant framework can be produced dominantly through the dijet processes via vector-boson fusion, especially when investigating them with strong experimental cuts. On the contrary, the dijet processes cannot be dominant anymore in the hypercharge anapole DM case because not only the γ exchange diagram but also Z-boson exchange diagram contribute to the process, leading to a quite significant cancellation in the high-energy regime so that the unitarity problem is diminished extremely efficiently [11]. As a result, the strongest LHC constraints on the hypercharge anapole DM couplings are expected to come from the so-called monojet processes $pp \to j + X$ with X standing for the collection of invisible particles including two DM particles, $\chi\chi$.

Two parton-level processes, $gq \to q\chi\chi$ and $q\bar{q} \to g\chi\chi$, contribute dominantly to the monojet process $pp \to j + X$ at the LHC. Quantitatively, the former gq cross section is much larger than the latter $q\bar{q}$ cross section. In this light, we consider the process $gq \to q\chi\chi$ in the present work as the most crucial mode for investigating the constraints from the LHC monojet events on the couplings versus the DM mass m_χ in the spin-1/2, 1, 3/2, and 2 cases.[4] There are two Feynman diagrams contributing to the sequential process $gq \to q\gamma^*/Z^* \to q\chi\chi$, of which one is a s-channel quark-exchange mode and the other a t-channel quark-exchange mode as depicted in Fig. 4. As demonstrated in all the DM annihilation processes in Sec. III, the effective anapole three-point $\gamma\chi\chi$ and $Z\chi\chi$ vertices allow each parton-level cross section to be completely factored into the SM 2-to-2 scattering process $gq \to q\gamma^*/Z^*$ and the DM pair production processes through the 2-body decay $\gamma^*/Z^* \to \chi\chi$. After performing the 2-body phase space integration over the invisible final two-body $\chi\chi$ system, we can obtain the parton-level cross section for the process $gq \to q\chi\chi$ in a compact integral form as

$$\sigma_{1/2}(\hat{s}; p_T) = \int_{4m_\chi^2}^{\hat{s}} \frac{dQ^2}{2\pi}\mathcal{O}(\hat{s}, Q^2; p_T)\frac{|a_{1/2}|^2}{\Lambda^4}, \tag{4.1}$$

[4]The parton-level process $g\bar{q} \to \bar{q}\chi\chi$ contributes to the same single-jet process at the LHC, although this mode is insignificant because the antiquark contribution is much smaller than the quark contribution to the parton distribution functions of the proton.

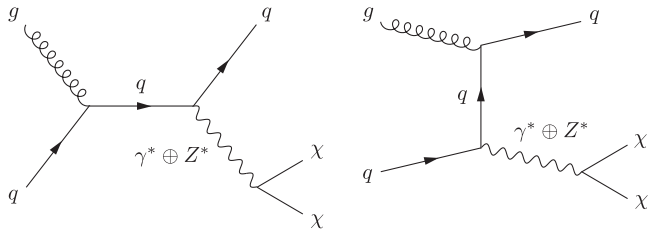

FIG. 4. Two parton-level Feynman diagrams contributing to the process $gq \to q\chi\chi$, of which the left one is for a s-channel quark exchange and the right one is for a t-channel quark exchange. If the quark mass is ignored, the t-channel diagram has a forward singularity to be regularized. The notation $\gamma^* \oplus Z^*$ stands for the combined s-channel γ and Z exchanges.

$$\sigma_1(\hat{s}; p_T) = \int_{4m_\chi^2}^{\hat{s}} \frac{dQ^2}{2\pi} \mathcal{O}(\hat{s}, Q^2; p_T) \left(\frac{Q^2}{4m_\chi^2}\right) \frac{|a_1|^2\beta_\chi^2 + |b_1|^2}{\Lambda^4}, \tag{4.2}$$

$$\sigma_{3/2}(\hat{s}; p_T) = \int_{4m_\chi^2}^{\hat{s}} \frac{dQ^2}{2\pi} \mathcal{O}(\hat{s}, Q^2; p_T) \left(\frac{Q^2}{4m_\chi^2}\right)^2 \times \frac{2|a_{3/2}|^2}{9\Lambda^4}(5 - 2\beta_\chi^2 + 5\beta_\chi^4), \tag{4.3}$$

$$\sigma_2(\hat{s}; p_T) = \int_{4m_\chi^2}^{\hat{s}} \frac{dQ^2}{2\pi} \mathcal{O}(\hat{s}, Q^2; p_T) \left(\frac{Q^2}{4m_\chi^2}\right)^3 \times \frac{1}{12\Lambda^4}[|a_2|^2\beta_\chi^2(7 - 6\beta_\chi^2 + 15\beta_\chi^4) + |b_2|^2(15 - 6\beta_\chi^2 + 7\beta_\chi^4)], \tag{4.4}$$

for the spin-1/2, -1, -3/2, and -2 cases, respectively, with the $\chi\chi$ invariant mass $\sqrt{Q^2}$ corresponding to the virtual γ^* or Z^* invariant mass, the speed factor $\beta_\chi = \sqrt{1 - 4m_\chi^2/Q^2}$ and the gq collision CM energy $\sqrt{\hat{s}}$ and the transverse-momentum cut p_T of the produced quark, invariant under any Lorentz boost along the proton beam direction. The parton-level 2-to-2 scattering processes $gq \to q\gamma^*/Z^*$ are encoded fully in the $\hat{s}$ and Q^2 dependent cross section $\mathcal{O}$. Explicitly, the parton-level effective cross section $\mathcal{O}$ with the transverse-momentum cut p_T is given by

$$\mathcal{O}(\hat{s}, Q^2; p_T) = \frac{e^2 g_S^2}{192\pi^2 c_W^2 \hat{s}}(|\bar{V}_q|^2 + A_q^2) Q^2 \Pi_Z(Q^2) \times \left(1 - \frac{4m_\chi^2}{Q^2}\right)^{3/2} \mathcal{F}(\hat{s}, Q^2; p_T), \tag{4.5}$$

with the strong-interaction coupling g_s, the normalized propagator $\Pi_Z(Q^2)$, and the modified vector coupling $\bar{V}_q$ of the quark q defined in Eqs. (3.8) and (3.9), where the parton-level q transverse momentum, which is invariant under the Lorentz boost along the beam direction, is $\hat{p}_T = \frac{\sqrt{\hat{s}}}{2}(1 - Q^2/\hat{s}) \sin\theta$ with the polar-angle θ between the momenta of the initial gluon g and the final quark q. The function $\mathcal{F}(\hat{s}, Q^2; p_T)$ with the transverse-momentum cut p_T in Eq. (4.5) is given explicitly by

$$\mathcal{F}(\hat{s}, Q^2; p_T) = \left(\frac{1}{3\sqrt{\hat{s}}} + \frac{Q^2}{\hat{s}^{3/2}}\right)\sqrt{p_{T\max}^2 - p_T^2} + \left(\frac{4p_{T\max}^2}{3\hat{s}} + \frac{Q^4}{3\hat{s}^2}\right) \ln\left(\frac{p_{T\max} + \sqrt{p_{T\max}^2 - p_T^2}}{p_T}\right) \sim \frac{1}{6}\left(1 + 2\frac{Q^2}{\hat{s}} - 3\frac{Q^2}{\hat{s}}\right) + \frac{1}{3}\left(1 - 2\frac{Q^2}{\hat{s}} + 2\frac{Q^4}{\hat{s}^2}\right) \ln\left(\frac{\hat{s} - Q^2}{\sqrt{\hat{s}} p_T}\right) \quad \text{for } p_T \to 0, \tag{4.6}$$

with the maximal transverse momentum $p_{T\max} = \frac{\sqrt{\hat{s}}}{2}(1 - Q^2/\hat{s})$. The transverse-momentum cut p_T is introduced to regularize the forward singularity caused by neglecting the quark mass; this also allows us to ignore particles escaping detection along the proton-beam pipe directions. Compared to the spin-1/2 case, the parton-level production cross section in the spin-1 case has an additional kinematic enhancement factor $Q^2/4m_\chi^2$ originating from the longitudinal mode of one of the two spin-1 DM particles as in Eq. (4.2). We note in passing that the power of the enhancement factor gets bigger for higher-spin cases due to the larger number of longitudinal modes so that the monojet searches at the LHC impose much stronger constraints on the couplings gradually. Certainly, the parton-level cross sections should be folded with proper quark and gluon parton distribution functions for evaluating the monojet cross section at the LHC.

In this paper, we adopt a simple statistical analysis for deriving the LHC and HL-LHC limits on the hypercharge anapole couplings versus the DM mass, focusing on the effective characterization of the hypercharge anapole DM particle according to the spin. Let us calculate the simplest version of the signal significance z defined by

$$z = \frac{s}{\sqrt{s + b}}, \tag{4.7}$$

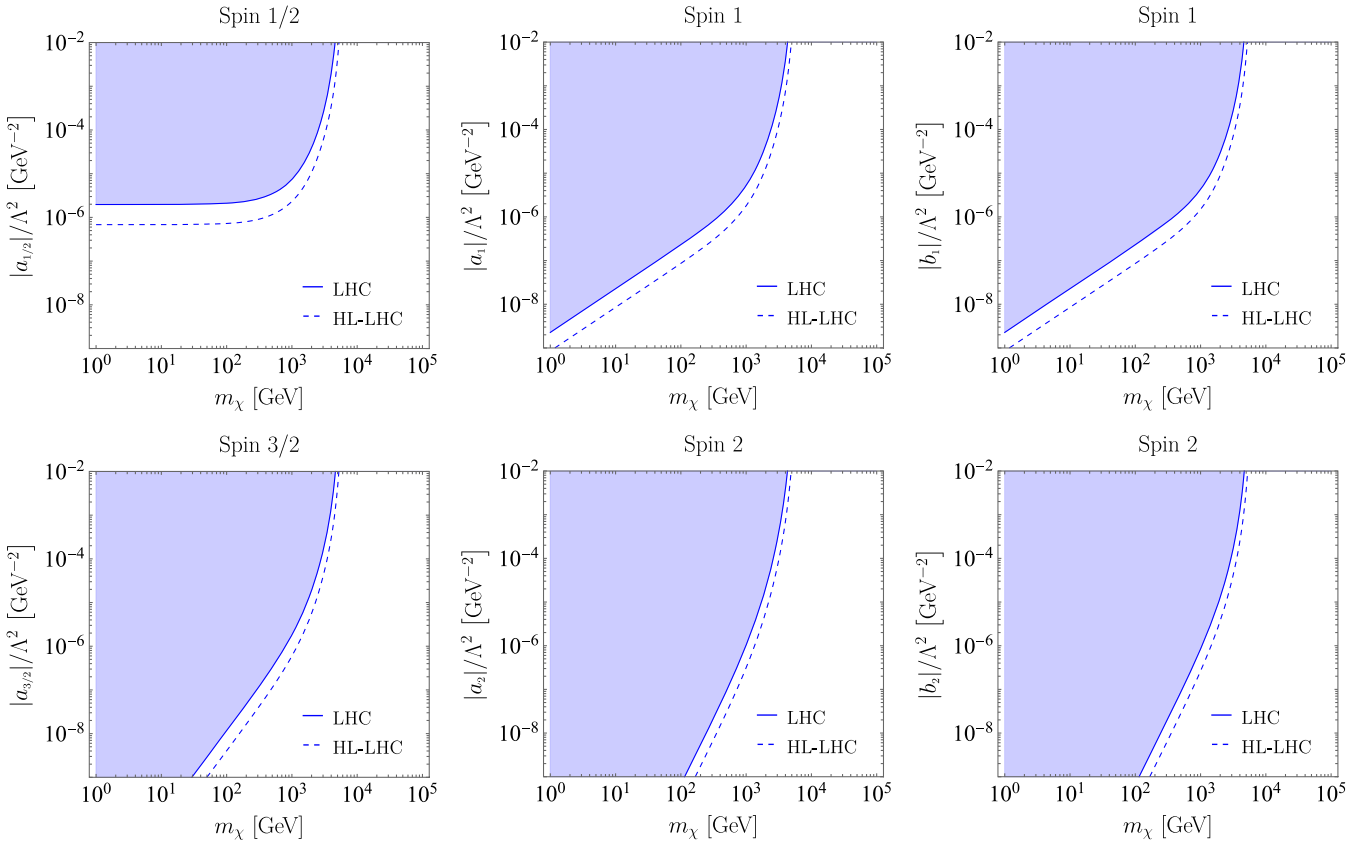

FIG. 5. Exclusion limits from the monojet events at the LHC (solid line) of 13 TeV energy and 139 fb^{-1} luminosity and projected sensitivities from those at the HL-LHC (dashed line) of 14 TeV energy and 3 ab^{-1} luminosity, respectively, derived mainly from the parton-level process $gq \to q\chi\chi$, on the effective couplings and the DM mass m_χ. The top (bottom) left panel shows the limits on the normalized coupling $a_{1/2}/\Lambda^2$ ($a_{3/2}/\Lambda^2$) in the spin-1/2 (spin-3/2) case. The top (bottom) middle panel shows the limits on the normalized coupling a_1/Λ (a_2/Λ^2) and the top (bottom) right panel shows the limits on the normalized coupling b_1/Λ^2 (b_2/Λ^2) in the spin-1 (spin-2) case.

with the numbers s and b of the signal and background events.[5] We set the critical significance value $z = 2$ to determine the 95% confidence level (CL) exclusion limits on the couplings normalized to the cutoff scale squared Λ^2. The events are selected according to the selection criteria $p_T^{\rm jet} > 250$ GeV and $|\eta| < 2.5$, applied to the most recent monojet searches with an integrated luminosity of 139 fb^{-1} at the LHC energy of 13 TeV by the ATLAS Collaboration in Ref. [77].

Figure 5 show the current exclusion limits from the LHC (shaded region bounded by the solid lines) and the expected sensitivities at the HL-LHC with the full running of the 3 ab^{-1} integrated luminosity (dashed lines). Comparing the panels from the top left one, it is clearly seen that the couplings in the higher-spin cases are constrained more strongly in the whole kinematically available region due to the higher power of the enhancement factor $Q^2/4m_\chi^2$, especially in the low mass region as indicated in Eqs. (4.2)–(4.4).

Close to the kinematical end point of the mass $m_\chi \sim 6$ TeV, there is a slight reduction in the a_1/Λ^2 (a_2/Λ^2) constraint compared to the b_1/Λ^2 (b_2/Λ^2) constraint, due to the presence of the higher power of the kinematical suppression factor $\beta_\chi^2 = 1$–$4m_\chi^2/Q^2$ for $Q^2 \sim 4m_\chi^2$ in the spin-1 (spin-2) case.

The dashed line in each panel shows the future sensitivity of the planned HL-LHC experiment with a slightly larger collision energy of 14 TeV and an integrated luminosity of 3 ab^{-1}, roughly 10 times larger than the present LHC luminosity [76,79]. We require slightly stronger selection criteria of the monojet events for the HL-LHC: $p_T^{\rm jet} > 300$ GeV and $|\eta| < 2.5$. As for the number of background events at $\sqrt{s} = 14$ TeV, we consider the difference in the cross sections of the dominant background process $pp \to Zj \to \nu\bar{\nu}j$, enhanced by $11.57/9.88 \approx 1.17$ compared to the $\sqrt{s} = 13$ TeV case [91].

[5]The most significant parton-level background process is $gq \to q\nu\bar{\nu}$ with two invisible neutrinos in the final state produced via a Z-boson exchange.

The projected sensitivities become stronger as m_χ decreases. Because of the Q^2 dependence of the $gq \to q\chi\chi$ production cross section, we expect that the 100 TeV future circular collider experiment under R&D [93,94] enables us to cover a much larger region of the couplings versus the anapole DM mass.

Before closing this section, we emphasize once more that the power of the invariant mass square in the monojet cross section increases in proportion to the spin value of the anapole DM particle. The enhancement arises from the increased number of longitudinal modes of the higher-spin anapole DM particle. It strongly indicates that the constraints on the couplings versus the DM mass from the LHC and HL-LHC monojet searches become much stronger as the spin value of the anapole DM particle increases.

V. DM DIRECT DETECTION

In this section, we describe how the exclusion limits on the hypercharge anapole DM couplings versus the DM mass are extracted from the recent DM direct detection experiment XENONnT with the 1.1 ton-yr exposure [75], which is at present the most powerful DM direct detection experiment. Along with the exclusion limits, we consider the projected sensitivities of the future XENONnT with the 20 ton-yr exposure. Nonrelativistic dark matter is assumed to move with a typical velocity of order $v \simeq 10^{-3}c$ in the Galactic halo.[6] Thus, the recoil energy of a DM particle against a heavy target nucleus is expected to be in the keV energy scale, much smaller than the typical DM mass $\gtrsim \mathcal{O}(\mathrm{GeV})$ in consideration here as well as the Z-boson mass $m_Z = 91.2$ GeV. Hence, the Z-boson exchange contribution to the elastic DM scattering off the target nucleus can be safely ignored because the momentum transfer is significantly smaller than the Z-boson mass m_Z and the DM scattering off the nucleus is dominated by the photon exchange [11].

Taking the small recoil energy limit and ignoring the Z-boson exchange contribution safely we can cast the recoil-energy-dependent differential cross section into the factorized form

$$\frac{d\sigma_{1/2}}{dE_R} = \frac{c_W^2 e^2}{4\pi^2}\frac{|a_{1/2}|^2}{\Lambda^4}\mathcal{A}(E_R), \tag{5.1}$$

$$\frac{d\sigma_1}{dE_R} = \frac{c_W^2 e^2}{6\pi^2}\frac{1}{\Lambda^4}\left[|a_1|^2\left(1+\frac{m_T E_R}{2m_\chi^2}\right)+|b_1|^2\frac{m_T E_R}{2m_\chi^2}\right]\mathcal{A}(E_R), \tag{5.2}$$

$$\frac{d\sigma_{3/2}}{dE_R} = \frac{5c_W^2 e^2}{36\pi^2}\frac{|a_{3/2}|^2}{\Lambda^4}\mathcal{A}(E_R), \tag{5.3}$$

$$\frac{d\sigma_2}{dE_R} = \frac{c_W^2 e^2}{120\pi^2}\frac{1}{\Lambda^4}\left[15|a_2|^2\left(1+\frac{13m_T E_R}{10m_\chi^2}\right)+7|b_2|^2\frac{m_T E_R}{2m_\chi^2}\right]\mathcal{A}(E_R), \tag{5.4}$$

for the spin-1/2, -1, -3/2, and -2 cases, respectively, with the target nucleus mass m_T and the recoil energy E_R. Note that the momentum transfer $q = \sqrt{2m_T E_R}$ is much smaller than our dark matter mass in consideration. One noteworthy feature is that the recoil-energy-dependent function $\mathcal{A}(E_R)$ is factored out independently of the spin of the anapole DM particle,

$$\mathcal{A}(E_R) = Z_T^2\left[2m_T - \left(1+\frac{m_T}{m_\chi}\right)^2\frac{E_R}{v_\chi^2}\right]F_C^2(q^2) + \frac{2m_T^2}{3m_p^2}\left(\frac{\bar{\mu}_T}{\mu_p}\right)^2\frac{E_R}{v_\chi^2}F_M^2(q^2), \tag{5.5}$$

with the atomic number Z_T of the target nucleus and the DM particle speed v_χ relative to the nucleus. The charge form factor F_C is given by

$$F_C(q^2) = \left(\frac{3j_1(qr_C)}{qr_C}\right)e^{-q^2s^2/2}, \tag{5.6}$$

in terms of the first-kind spherical Bessel function j_1 of order 1 where $r_C = (c^2 + 7\pi^2a^2/3 - 5s^2)^{1/2}$ with $c \simeq (1.23A^{1/3} - 0.60)$ fm, $a \simeq 0.52$ fm, and $s \simeq 0.9$ fm, and the atomic mass A of the target nucleus, while the magnetic dipole moment form factor F_M [99,100] is given by

$$F_M(q^2) = \begin{cases} \frac{\sin(qr_M)}{qr_M} & \text{for } qr_M < 2.55, qr_M > 4.5, \\ 0.2168 & \text{for } 2.55 < qr_M < 4.5, \end{cases} \tag{5.7}$$

with the radius $r_M = 1.0A^{1/3}$ fm. The recoil-energy-dependent function $\mathcal{A}$ in Eq. (5.5) involves the nuclear magneton $\mu_p = e/2m_p$ with the proton mass m_p and the weighted dipole moment $\bar{\mu}_T$ for the target nuclei [101],

$$\bar{\mu}_T = \left(\sum_i f_i\mu_i^2\frac{s_i+1}{s_i}\right)^{1/2}, \tag{5.8}$$

where f_i, μ_i, and s_i are the abundance fraction, magnetic moment, and spin of the isotope i.

The recoil-energy-dependent distribution of the DM direct detection process is given by integrating the differential cross section of each DM spin as in Eqs. (5.1)–(5.4) over the DM velocity with the distribution $f_{\mathrm{LAB}}(\vec{v})$ in the laboratory frame as

[6]Note that the scenarios with fast-moving light DM, so-called *boosted dark matter*, are proposed in Refs. [95–98], but they are not the majority of the cosmological DM with the observed relic abundance.

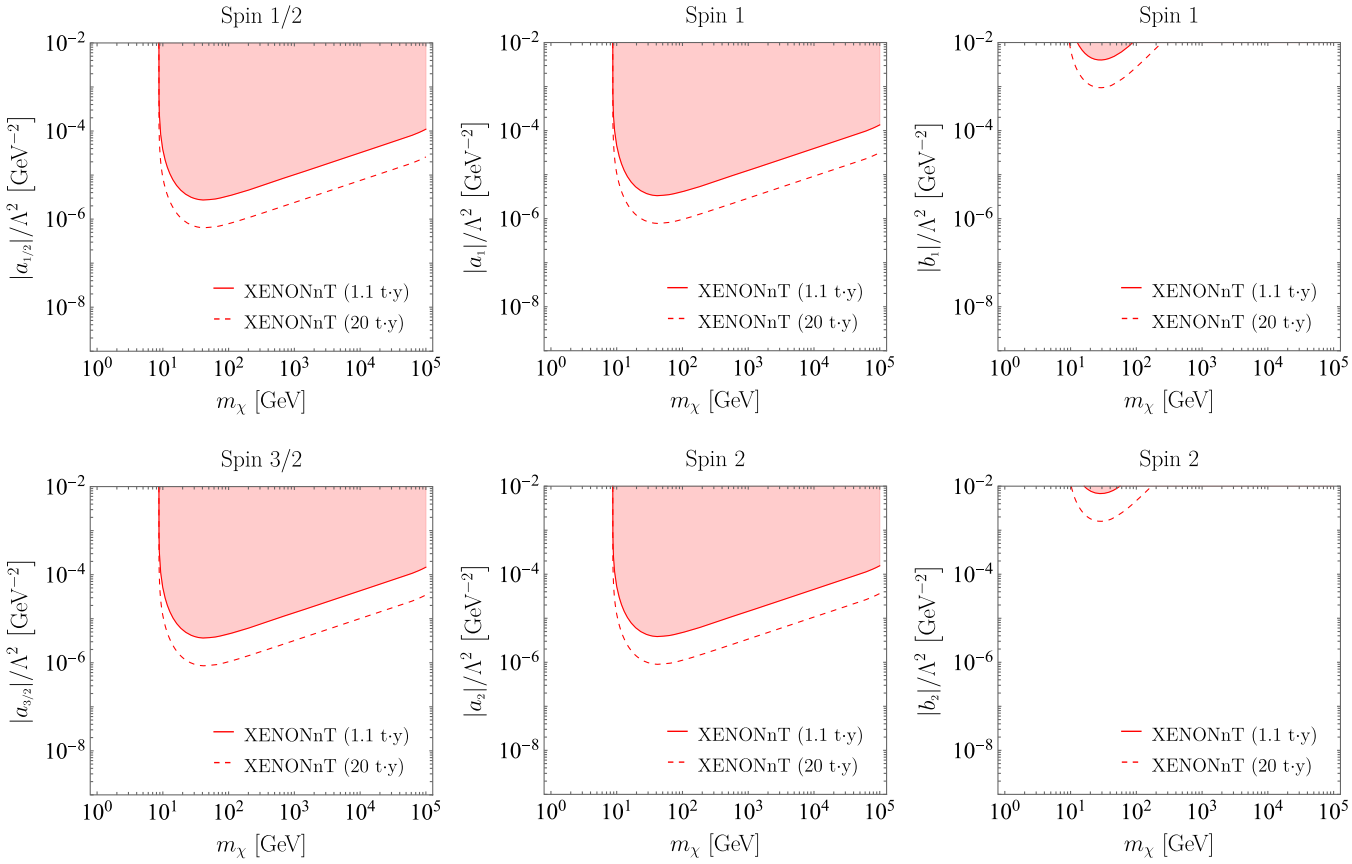

FIG. 6. Exclusion limits from the DM direct detection experiment XENONnT on the effective couplings versus the DM mass m_χ. The solid line is the current limit with the 1.1 ton-yr exposure, and the dashed line is the expected sensitivity with the 20 ton-yr exposure. The top (bottom) left panel shows the limit on the normalized coupling $|a_{1/2}|/\Lambda^2$ ($|a_{3/2}|/\Lambda^2$) versus the DM mass in the spin-1/2 (spin-3/2) case. The top (bottom) middle panel shows the limit on the normalized coupling $|a_1|/\Lambda^2$ ($|a_2|/\Lambda^2$) versus the DM mass in the spin-1 (spin-2) case while setting the other coupling to zero. The top (bottom) right panel show the limit on the normalized coupling $|b_1|/\Lambda^2$ ($|b_2|/\Lambda^2$) versus the DM mass in the spin-1 (spin-2) case while setting the other coupling to zero. The right panels clearly show that the normalized couplings, $|b_1|/\Lambda^2$ and $|b_2|/\Lambda^2$, for the spin-1 and spin-2 DM cases get much weaker constraints than the other cases.

$$\frac{dR}{dE_R} = \frac{1}{m_T}\frac{\rho_{\rm loc}}{m_\chi}\int d^3\vec{v}|\vec{v}|f_{\rm LAB}(\vec{v})\frac{d\sigma}{dE_R}, \tag{5.9}$$

where we use the local DM density $\rho_{\rm loc} = 0.3\ {\rm GeV\,cm^{-3}}$. In the present work, we adopt a simple Maxwell-Boltzmann distribution in the Galactic frame truncated at the escape speed $v_{\rm esc}$ of our Galaxy,

$$f_{\rm LAB}(\vec{v}) = f(\vec{v}+\vec{v}_{\rm E}), \tag{5.10}$$

with the velocity $\vec{v}_{\rm E}$ of the Earth in the Galactic frame and

$$f(\vec{v}) = \begin{cases} \frac{1}{\mathcal{N}} e^{-v^2/v_0^2} & \text{for } |\vec{v}| \le v_{\rm esc}, \\ 0 & \text{for } |\vec{v}| > v_{\rm esc}, \end{cases} \tag{5.11}$$

where the normalization constant $\mathcal{N}$ is

$$\mathcal{N} = (\pi v_0^2)^{3/2}\left[{\rm erf}\left(\frac{v_{\rm esc}}{v_0}\right) - \frac{2}{\sqrt{\pi}}\frac{v_{\rm esc}}{v_0}e^{-v_{\rm esc}^2/v_0^2}\right],$$

with the error function ${\rm erf}(z) = 2\int_0^z e^{-t^2}dt/\sqrt{\pi}$. The values of the three different speeds are set numerically to the escape speed $v_{\rm esc} = 544\ {\rm km\,s^{-1}}$, the speed of the Sun relative to the DM reference frame $v_0 = 220\ {\rm km\,s^{-1}}$, and the Earth speed $v_E = 232\ {\rm km\,s^{-1}}$ in the Galactic frame.

By integrating out the recoil-energy distribution dR/dE_R in Eq. (5.9) and taking into account the detection efficiencies of the XENONnT experiment [75], we can evaluate the number of recoil DM detection events. For the details of calculating the expected signal events, we refer to Appendix B of Ref. [71]. The top (bottom) left panel of Fig. 6 shows the 90% CL constraint on the normalized coupling $|a_{1/2}|/\Lambda^2$ ($|a_{3/2}|/\Lambda^2$) versus the DM mass m_χ in the spin-1/2 (spin-3/2) case. The top (bottom) middle panel shows the constraint on the normalized coupling $|a_1|/\Lambda^2$ ($|a_2|/\Lambda^2$) versus m_χ, and the top (bottom) right panel shows the constraint on the normalized coupling $|b_1|/\Lambda^2$ ($|b_2|/\Lambda^2$) versus m_χ in the spin-1 (spin-2) case. In each plot, the excluded region of the corresponding

coupling versus the DM mass is shown as the red-shaded area bounded by the exclusion limit with a red solid line. Note that each of the second terms proportional to the recoil energy E_R on the couplings, $|a_1|/\Lambda^2$ and $|a_2|/\Lambda^2$ in Eqs. (5.2) and (5.4), is much smaller than unity, i.e., $m_T E_R/(2m_\chi^2) \ll 1$, and hence the direct detection bounds on the $|a_i|/\Lambda^2$ couplings with $i = 1/2, 1, 3/2, 2$ are dominantly determined by the spin-averaged factors. On the other hand, the direct detection cross sections are suppressed by $m_T E_R/2m_\chi^2$ once they are dominated by the $|b_i|/\Lambda^2$ term with $i = 1, 2$, which results in the negligible sensitivities as shown in the right panels. The tiny difference between the limits on the couplings, $|b_1|/\Lambda^2$ and $|b_2|/\Lambda^2$, arise from the different spin-averaged and polarization-weighted factors, $1/6$ and $7/120$, in the detection rates, respectively. For the expected sensitivities of the upcoming XENONnT with the 20 ton-yr exposure shown with the dashed lines, we relied simply on scaled statistics without accounting for potential future improvements in background rejection and the control of systematic uncertainties.

As shown previously in Fig. 5, the LHC and HL-LHC monojet constraints on the couplings of a lower-spin particle are much weaker than those on the couplings of a higher-spin case, especially for the DM mass $m_\chi \lesssim 1$ TeV. Hence, the LHC/HL-LHC and DM direct detection experiments can play quite complementary roles in imposing the exclusion limits on the couplings versus the DM mass.

VI. COMBINED CONSTRAINTS AND FUTURE SENSITIVITIES

In this section, we show the results combining all the aforementioned experimental constraints and future sensitivities on the effective couplings versus the DM mass coming from the Planck determination of the DM relic abundance, the LHC and HL-LHC monojet searches, and the present DM direct detection experiment XENONnT and its future data of 20 ton·yr exposure, which have been evaluated systematically in the previous three sections. On top of those experimental bounds and sensitivities, we include an additional theoretical constraint from the NPB for guaranteeing the validity of the EFT formalism, which needs to be taken with a grain of salt.[7] The energy-dependent NPBs on the couplings simply read

$$\frac{|a_{1/2}|}{\Lambda^2} s \le 4\pi, \qquad \frac{\sqrt{|a_1|^2+|b_1|^2}}{\Lambda^2} s \le 4\pi,$$
$$\frac{|a_{3/2}|}{\Lambda^2} s \le 4\pi, \quad \text{and} \quad \frac{\sqrt{|a_2|^2+|b_2|^2}}{\Lambda^2} s \le 4\pi, \tag{6.1}$$

for the spin-1/2, -1, -3/2, and -2 cases, respectively. As the CM energy $\sqrt{s} \ge 2m_\chi$, the NPB condition (6.1) applied to the asymptotically high-energy limit leads to the inequality relations

$$\frac{|a_{1/2}|}{\Lambda^2} \le \frac{\pi}{m_\chi^2}, \qquad \frac{\sqrt{|a_1|^2+|b_1|^2}}{\Lambda^2} \le \frac{\pi}{m_\chi^2},$$
$$\frac{|a_{3/2}|}{\Lambda^2} \le \frac{\pi}{m_\chi^2}, \quad \text{and} \quad \frac{\sqrt{|a_2|^2+|b_2|^2}}{\Lambda^2} \le \frac{\pi}{m_\chi^2}, \tag{6.2}$$

on the effective couplings versus the DM mass m_χ. The imposition of those constraints is a very loose statement on the tree-level perturbativity. If the limits are violated, we naively expect that higher-loop corrections must be included, which is beyond the scope of this paper.

Figure 7 shows the combined exclusion limits on the effective normalized couplings versus the anapole DM mass m_χ from the Planck measurement of the DM relic abundance (black solid), the theoretical NPB condition (orange solid), the monojet searches at the LHC of 13 TeV with the integrated luminosity of 139 fb^{-1} (blue solid) and the full running of the HL-LHC of 14 TeV with the 3 ab^{-1} integrated luminosity (blue dashed), and the present DM direct detection experiment XENONnT (red solid) with the 1.1 ton-yr exposure along with the future XENONnT with the 20 ton-yr exposure (red dashed). The top (bottom) left panel is the combined constraint on the normalized coupling $|a_{1/2}|/\Lambda^2$ ($|a_{3/2}|/\Lambda^2$) versus the mass m_χ in the spin-1/2 (spin-3/2) case. The top (bottom) middle panel shows the combined limit on the normalized coupling $|a_1|/\Lambda^2$ ($|a_2|/\Lambda^2$), and the top (bottom) right panel shows the combined limit on the normalized coupling $|b_1|/\Lambda^2$ ($|b_2|/\Lambda^2$) versus m_χ in the spin-1 (spin-2) case. Note that the future sensitivities of XENONnT can be reached within about 5 years of running or the XLZD consortium of many Xenon target experiment plans [102].

In the spin-1/2 case, two regions are still allowed. One tiny allowed region is near the Z pole with $m_\chi = m_Z/2$, where the relic abundance constraint becomes much weaker due to the sharp Z-resonance effect. This tiny region is expected to be completely excluded by the upcoming DM direct detection experiments and the HL-LHC experiment, as indicated by the red and blue dashed lines. The other allowed region is a triangle-shape area centered near $|a_{1/2}|/\Lambda^2 = 10^{-6}$ GeV^{-2} and $m_\chi = 1$ TeV, nearly half of which can be probed in the near future by XENONnT after the 20 ton·yr exposure. This shows the effectiveness of the complementary DM EFT approach.

[7] As the anapole terms are described by an effective Lagrangian with higher-dimensional terms, the so-called tree-level unitarity is violated in the high-energy regime as well in various processes such as $\chi\chi \to W^-W^+$. However, quantitatively the combined constraint from the tree-level unitarity condition turns out to be much weaker than that from the naive perturbativity condition.

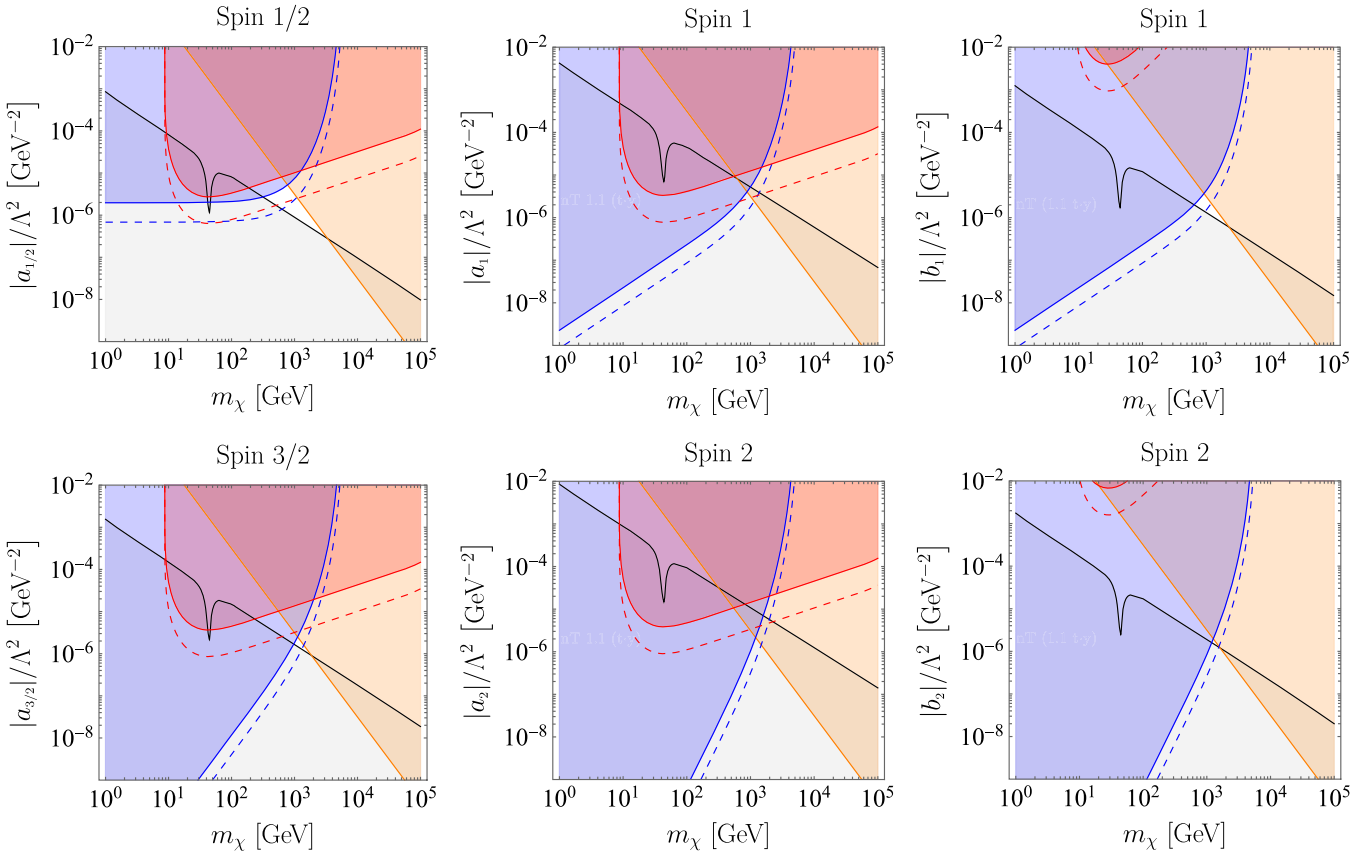

FIG. 7. Combined exclusion limits on the effective couplings versus the DM mass m_χ from the measured DM relic abundance of the Planck satellite (black solid), the theoretical NPB (orange solid), the LHC (blue solid) and HL-LHC (blue dashed) monojet search experiments and the DM direct detection experiment XENONnT current limit with the 1.1 ton-yr exposure (red solid) and the future prospect with the 20 ton-yr exposure (red dashed). The top (bottom) left panel shows the combined constraint on the normalized coupling $|a_{1/2}|/\Lambda^2$ ($|a_{3/2}|/\Lambda^2$) versus the DM mass in the spin-1/2 (spin-3/2) case. The top (bottom) middle panel shows the combined constraint on the normalized coupling $|a_1|/\Lambda^2$ ($|a_2|/\Lambda^2$) versus the DM mass, and the top (bottom) right panel shows the combined constraint on the normalized coupling $|b_1|/\Lambda^2$ ($|b_2|/\Lambda^2$) versus the DM mass in the spin-1 (spin-2) case, while setting the other coupling to zero.

In the spin-1 case, the Z-resonance region with $m_\chi \simeq m_Z/2$ is entirely ruled out by the combined constraints arising from both relic abundance measurements and LHC search experiments, illustrated in the upper middle and right frames of Fig. 7. This complete exclusion arises from two synergistic effects, independent of the constraints posed by both the DM direct detection experiment and the NPB bound. Compared to the spin-1/2 case, the relic abundance constraint is bolstered by 1.5 times, attributed to a smaller spin-averaged factor than that in the spin-1/2 case. Furthermore, the constraints imposed by the LHC experiments are significantly heightened, primarily due to the longitudinal mode of the spin-1 DM particle, particularly noticeable for m_χ less than 1 TeV. Moreover, the spin-1 case with a nonzero $|a_1|$ but $|b_1| = 0$ is expected to face total exclusion, as depicted in the top middle panel of Fig. 7. Here, the combined constraints from relic abundance measurements, the (HL-)LHC and (upgraded) DM direct detection experiments, and the theoretical NPB synergistically contribute to this complete exclusion. Conversely, the spin-1 case with a nonzero $|b_1|$ but $|a_1| = 0$ features a triangular-shaped allowed region centered around $|b_1|/\Lambda^2 = 10^{-6}$ GeV^{-2} and $m_\chi = 1, \mathrm{TeV}$, even though the permitted area is substantially reduced compared to the spin-1/2 scenario, due to the much more strengthened constraints from the relic abundance and LHC experiment. While the complete HL-LHC operational phase is not anticipated to entirely cover this small permissible region, the future 100 TeV circular pp collider [93] promises the capability to thoroughly investigate and potentially close off the remaining segments of this area, because of its vastly greater collision energy and significantly improved sensitivity.

Despite the slightly weaker XENONnT constraints on the coupling $|a_{3/2}|/\Lambda^2$ in the spin-3/2 case than the smaller spin cases due to the spin-averaged and polarization-weighted factors, the currently allowed parameter region is smaller. This is because the LHC constraint gets much

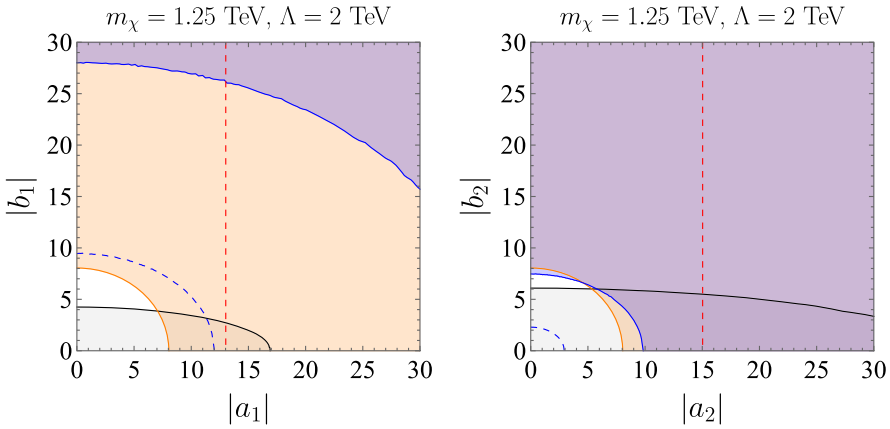

FIG. 8. The parameter spaces of two couplings, $|a_1|$ and $|b_1|$ (left), and two couplings, $|a_2|$ and $|b_2|$ (right), for the specific values of the DM particle mass, $m_\chi = 1.25$ TeV, and the cutoff scale, $\Lambda = 2$ TeV, in the spin-1 and -2 cases, respectively. The red and blue dashed lines indicate the projected sensitivities from the XENONnT with the 20 ton-yr exposure and the HL-LHC experiment after the full running with the integrated luminosity of 3 ab^{-1}, respectively.

stronger stemming from the enhancement of the monojet production cross section by the larger number of longitudinal modes as explained in Sec. IV.

The full running of the HL-LHC is expected to probe nearly half or more of the very tiny allowed regions. This effect leads to a remarkable result for the higher spin case, i.e., spin-2 DM. As shown in the bottom-middle and bottom-right panels, the LHC monojet searches so far have provided extremely strong constraints: full exclusion for the $|a_2|/\Lambda^2$ dominated case and nearly exclusion except for the region $m_\chi \sim 1.2$ TeV for the $|b_2|/\Lambda^2$ dominated case. The remaining region is expected to be fully probed at the HL-LHC in particular with more effective search strategies. Because of the gradual tightening of constraints from relic abundance and LHC data for higher-spin cases, it becomes evident that all hypercharge anapole dark matter particles with masses below the GeV scale are excluded, irrespective of their spin values, provided they adhere to the thermal freeze-out scenario.

To cover a general model setup for spin-1 and -2 DM including both non-negligible parity odd terms ($|a_{1,2}|/\Lambda^2$) and even terms ($|b_{1,2}|/\Lambda^2$) in the cross sections, we display the combined constraints and sensitivities in the two-dimensional ($|a_i|$ and $|b_i|$) plane after fixing the DM mass $m_\chi = 1.25$ TeV and the cutoff scale $\Lambda = 2$ TeV in Fig. 8. Each of the constraints is given by an ellipse due to the cross sections being proportional to the combination of the absolute squares of two couplings in the spin-1 and spin-2 cases. We ignore the constraints on $|b_i|$ from XENONnT, which are too weak. The left panel is for the spin-1 DM, and the right panel is for the spin-2 DM. Note that the future XENONnT sensitivity with the 20 ton·yr exposure (red dashed vertical line) is comparable to those of the HL-LHC full running for the spin-1 DM, while the latter becomes more powerful for the spin-2 DM. We expect that a higher-spin $s > 2$ DM scenario would suffer from even stronger bounds, although further dedicated studies are needed. The right panel of Fig. 8 shows that the full running of the HL-LHC can probe fully the spin-2 scenario with $m_\chi = 1.25$ TeV.

VII. SUMMARY AND CONCLUSION

Our investigation focused on a scenario where DM is characterized as a Majorana particle possessing a nonzero spin, interacting solely with SM particles via hypercharge anapole terms. This scenario renders us to pursue the combined analysis from various experimental results in a complementary way via the EFT approach. For the experimental/observational constraints and sensitivities, we applied the Planck measurement of the DM relic abundance, the direct detection experiment XENONnT, and the LHC monojet searches together with the expected sensitivities at the HL-LHC and the future XENONnT. Because of the straightforward calculations and strong theoretical foundations, we conducted a focused numerical analysis on DM spins $s = 1/2$, 1, $3/2$, and 2, making comparative analyses among them for the first time within the realm of anapole DM studies. A succinct summary of the anapole Dark Matter scenarios and experimental searches analyzed in this paper is presented in Table I of the introduction section, juxtaposed with previous literature for comparison. The expectation for the higher-spin DM scenarios will be briefly discussed at the end of this section. Considering the theoretically allowed range of the EFT approach together with a grain of salt, we demonstrate that the hypercharge anapole DM scenarios are currently on the verge of being discovered or ruled out.

The main results of the present work can be summarized with the following key points:

(i) As easily expected, the relic abundance imposes stronger constraints on d-wave terms than the p-wave terms since larger couplings are required to obtain the right relic abundance. The overall

spin-averaged and polarization-weighted factors, which are 1/4 ($|a_{1/2}|$), 1/9 ($|a_1|$ and $|b_1|$), 5/72 ($|a_{3/2}|$), 7/300 ($|a_2|$), and 1/20 ($|b_2|$), in the annihilation cross sections decrease as the DM spin increases. This leads to stronger constraints for higher spin cases. In each case, the relic abundance constraint in the Z-pole resonance region is about a factor of 10 times weaker than the others.

(ii) The LHC and HL-LHC monojet searches play the most crucial role in probing the higher-spin anapole DM lighter than about 1 TeV. This is due to the kinematic factor associated with the longitudinal modes of the DM particle. The monojet searches play an essential role, especially for probing the parity-even terms of the spin 1 or 2 DM, i.e., $|b_{1,2}|/\Lambda^2$, since their contributions to the DM direct detection cross sections are suppressed by the recoil energies.

(iii) The momentum transfer in the DM direct detection process is sufficiently small, and hence the dominant contribution is through the t-channel photon exchange. The constraint on the parity-odd couplings $|a_{1/2}|/\Lambda^2$, $|a_1|/\Lambda^2$, $|a_{3/2}|/\Lambda^2$, and $|a_2|/\Lambda^2$ are comparable to each other, with minor deviations due to the spin-averaged and polarization-weighted factors, 1/2, 1/3, 5/18, and 1/4, respectively. The cross section, when considering only the spin-1 (spin-2) parity-even coupling $|b_1|/\Lambda^2$ ($|b_2|/\Lambda^2$), is suppressed in the nonrelativistic limit by the small kinetic factor due to the CP selection rule. Consequently, as illustrated in the top (bottom) right panel of Fig. 6, the constraint on $|b_1|/\Lambda^2$ ($|b_2|/\Lambda^2$) is highly suppressed by the recoil energy as $m_T E_R/2m_\chi^2$. It is noteworthy that the result from the near future XENONnT with the 20 ton-yr exposure is expected to explore the allowed region of space that coincides with the HL-LHC expectations for the spin-1/2 case, as shown in the top left panel of Fig. 7. Remarkably, the upcoming XENONnT experiment has the potential to achieve the extended coverage within approximately 5 years, which is significantly sooner than the projected full operational timeline of the HL-LHC. Thus, the future DM direct detection experiments, such as the planned XLZD consortium involving multiple Xenon target experiments with more than 20 ton-yr exposure, could eventually probe beyond the allowed region bounded by the HL-LHC expectation at a faster pace, in the spin-1/2 case.

(iv) The NPB condition is equally and approximately applied to all the spin-1/2, -1, -3/2, and -2 couplings. The lower NPB bound is inversely proportional to the square of the DM mass, as presented in Eq. (6.2). It is important to note that a breach of this conceptual NPB suggests a breakdown of the EFT framework, potentially resolvable by a more fundamental UV theory [13–15]. Hence, the NPB bounds need to be accepted cautiously.

Overall, the combined analysis shows that the hypercharge anapole coupling of a higher spin DM is more stringently constrained or expected to be probed sooner than that of a lower spin DM as evident in Fig. 7. We expect the 100 TeV proton-proton future circular collider (FCC) experiment, which is currently under R&D would have a potential to completely probe the whole remaining parameter space of the anapole DM scenarios considered here. Note that our analysis result combining the constraints from the observed relic abundance and the monojet searches at the LHC can be extended to a lighter DM mass down to $\mathcal{O}(10\ \mathrm{MeV})$ as long as the DM relic is determined by the freeze-out mechanism, providing a powerful exclusion bound already.

The DM particle with its spin larger than 2 is regarded to be innately a composite particle in order to avoid various conceptual problems such as unitarity issues. Nevertheless, if the scale of compositeness is significantly high, we expect that scenarios with spins greater than 2 could potentially be completely ruled out because of the substantial kinematic factor linked to an increased number of longitudinal modes of the DM particle in the anapole vertices. although no conclusive comments can be made yet before dedicated studies.

ACKNOWLEDGMENTS

This work is supported by the Basic Research Laboratory Program of the National Research Foundation of Korea (Grant No. NRF-2022R1A4A5030362 for S. Y. C., D. W. K., and S. S.). S. Y. C. is supported in part by the Basic Science Research Program of Ministry of Education through the National Research Foundation of Korea (Grant No. NRF-2022R1I1A3071226). S. S. is supported in part by the National Research Foundation of Korea (Grants No. NRF 2020R1I1A3072747). J. J. is supported by a KIAS Individual Grant (Grant No. QP090001) via the Quantum Universe Center at Korea Institute for Advanced Study. The hospitality of Asia Pacific Center for Theoretical Physics (APCTP) during the program "Dark Matter as a Portal to New Physics 2024" is kindly acknowledged.

APPENDIX A: ALGORITHM FOR CONSTRUCTING THE ANAPOLE VERTICES

This Appendix is devoted to a compact description of an efficient and systematic algorithm for constructing any U(1) gauge-invariant anapole vertex of a virtual gauge boson and two identical Majorana particles of any spin s.

Let us begin by constructing the wave tensor of a particle of nonzero mass m and any nonzero spin s. For a nonzero integer spin $s = n$, the wave function of an incoming massive boson with momentum k and helicity λ is given by a wave tensor defined as a product of n spin-1 polarization vectors by

$$\epsilon^{\alpha_1\cdots\alpha_n}(k,\lambda)=\sqrt{\frac{2^s(s+\lambda)!(s-\lambda)!}{(2s)!}}\sum_{\{\tau_i\}=-1}^{1}\delta_{\tau_1+\cdots+\tau_n,\lambda}\prod_{j=1}^{s}\frac{\epsilon^{\alpha_j}(k,\tau_j)}{\sqrt{2}^{|\tau_j|}}, \tag{A1}$$

and, for a half-integer spin $s=n+1/2$, the wave function of the massive fermion with momentum k and helicity λ is given by two types of wave tensors as

$$u^{\alpha_1\cdots\alpha_n}(k,\lambda)=\sum_{\tau=\pm1/2}\sqrt{\frac{s+2\tau\lambda}{2s}}\epsilon^{\alpha_1\cdots\alpha_n}(k,\lambda-\tau)u(k,\tau)\quad\text{with}\quad|\lambda-\tau|\le n, \tag{A2}$$

$$\bar{v}^{\alpha_1\cdots\alpha_n}(k,\lambda)=\sum_{\tau=\pm1/2}\sqrt{\frac{s+2\tau\lambda}{2s}}\epsilon^{*\alpha_1\cdots\alpha_n}(k,\lambda-\tau)\bar{v}(k,\tau)\quad\text{with}\quad|\lambda-\tau|\le n, \tag{A3}$$

with the helicity λ varying from $-s$ to s. The u tensor is for an incoming fermion and the $\bar{v}=v^\dagger\gamma^0$ tensor for an incoming antifermion.

The wave tensors have several characteristic features. The bosonic wave tensors are totally symmetric, traceless, and divergence free,

$$\varepsilon_{\mu\nu\alpha_i\alpha_j}\epsilon^{\alpha_1\cdots\alpha_i\cdots\alpha_j\cdots\alpha_s}(k,\lambda)=0, \tag{A4}$$

$$g_{\alpha_i\alpha_j}\epsilon^{\alpha_1\cdots\alpha_i\cdots\alpha_j\cdots\alpha_s}(k,\lambda)=0, \tag{A5}$$

$$k_{\alpha_i}\epsilon^{\alpha_1\cdots\alpha_i\cdots\alpha_s}(k,\lambda)=0, \tag{A6}$$

with $i,j=1,\ldots,n$, as indicated clearly by Eq. (A1), and the fermionic wave tensors satisfy the fermionic version of the divergence-free condition

$$\gamma_{\alpha_i}u^{\alpha_1\cdots\alpha_i\cdots\alpha_n}=\gamma_{\beta_i}v^{\beta_1\cdots\beta_i\cdots\beta_n}=0. \tag{A7}$$

These four properties of the wave tensors are very effective in constructing the general three-point vertices as well as the gauge-invariant ones as demonstrated in a series of works [85–90].

In the present work, we deal with the U(1) gauge-invariant anapole $\chi\chi B$ vertex of two Majorana particles of any spin and a virtual hypercharge gauge boson. The U(1) gauge invariance allows us to treat the virtual gauge boson B^* as an on-shell spin-1 particle of a varying mass m_*, as every term proportional to the 4-momentum appearing in the numerator of the propagator is effectively killed off. The DM pair annihilation is related to the amplitude for the s-channel annihilation process $\chi\chi\to B^*$ and the monojet events at the LHC and HL-LHC involve the decay process $B^*\to\chi\chi$, while the DM direct detection involves the t-channel transition $\chi\to\chi B^*$.

As all the three processes with different event topologies are related through crossing symmetry, it is sufficient to simply derive the covariant three-point vertex for the decay of a spin-1 particle B^* of mass m_* into two particles, χ_1 and χ_2, of identical spin s and mass m,

$$B^*(p,\sigma)\to\chi_1(k_1,\lambda_1)+\chi_2(k_2,\lambda_2), \tag{A8}$$

where p and σ are the B^* momentum and helicity and $k_{1,2}$ and $\lambda_{1,2}$ are the momenta and helicities of two χ particles. The corresponding helicity amplitudes can be written in the Jacob-Wick helicity formalism [103,104] as

$$\mathcal{M}^{B^*\to\chi_1\chi_2}_{\sigma;\lambda_1,\lambda_2}(\theta,\phi)=\mathcal{C}^1_{\lambda_1,\lambda_2}d^1_{\sigma,\lambda_1-\lambda_2}(\theta)e^{i(\sigma-\lambda_1+\lambda_2)\phi}\quad\text{with}\quad|\lambda_1-\lambda_2|\le1 \tag{A9}$$

$$=\bar{\psi}_1^{\alpha_1\cdots\alpha_n}(k_1,\lambda_1)\Gamma^{(s)}_{\alpha_1\cdots\alpha_n,\beta_1\cdots\beta_n;\mu}(p,q)\psi_2^{\beta_1\cdots\beta_n}(k_2,\lambda_2)\epsilon^\mu(p,\sigma), \tag{A10}$$

with the Wigner d function in Ref. [104] and the integer $n=s$ or $s-1/2$ for the bosonic or fermionic particle. In the bosonic case with $s=n$, the two spin-s wave tensors are

$$\bar{\psi}_1^{\alpha_1\cdots\alpha_n}(k_1,\lambda_1)=\epsilon^{*\alpha_1\cdots\alpha_n}(k_1,\lambda_1), \tag{A11}$$

$$\psi_2^{\beta_1\cdots\beta_n}(k_2,\lambda_2)=\epsilon^{*\beta_1\cdots\beta_n}(k_2,\lambda_2), \tag{A12}$$

which can be derived explicitly with the complex conjugation in Eq. (A1). In the fermionic case with $s=n+1/2$, the two spin-s wave tensors are

$$\bar{\psi}_1^{\alpha_1\cdots\alpha_n}(k_1,\lambda_1)=\bar{u}^{\alpha_1\cdots\alpha_n}(k_1,\lambda_1), \tag{A13}$$

$$\psi_2^{\beta_1\cdots\beta_n}(k_2,\lambda_2)=v^{\beta_1\cdots\beta_n}(k_2,\lambda_2), \tag{A14}$$

which can be derived explicitly by use of Eqs. (A2) and (A3).

Taking the procedure described in detail in Refs. [80,81], we can construct the covariant three-point vertex systematically. Before writing down them in a compact form, we introduce two fermionic basic operators defined by

$$P^{\pm} = \frac{1}{2}(1 \mp \kappa\gamma_5), \tag{A15}$$

$$W_{\mu}^{\pm} = \frac{1}{2}(\pm\kappa\gamma_{\perp\mu} + \gamma_{\mu}\gamma_5), \tag{A16}$$

where $\kappa = \sqrt{1-4m^2/m_*^2}$ and $\gamma_{\perp\mu} = g_{\perp\mu\nu}\gamma^{\nu}$ with the orthogonal tensor $g_{\perp\mu\nu} = g_{\mu\nu} - \hat{p}_{\mu}\hat{p}_{\nu} + \hat{q}_{\mu}\hat{q}_{\nu}$ and also four bosonic basic operators

$$S_{\alpha\beta}^{0} = \hat{p}_{\alpha}\hat{p}_{\beta}, \tag{A17}$$

$$S_{\alpha\beta}^{\pm} = \frac{1}{2}[g_{\perp\alpha\beta} \pm i\langle\alpha\beta\hat{p}\,\hat{q}\rangle], \tag{A18}$$

$$V_{1\alpha\beta;\mu}^{\pm} = \frac{1}{2}\hat{p}_{\beta}[g_{\perp\alpha\mu} \pm i\langle\alpha\mu\hat{p}\,\hat{q}\rangle], \tag{A19}$$

$$V_{2\alpha\beta;\mu}^{\pm} = \frac{1}{2}\hat{p}_{\alpha}[g_{\perp\beta\mu} \mp i\langle\beta\mu\hat{p}\,\hat{q}\rangle], \tag{A20}$$

with the totally antisymmetric tensor $\langle\alpha\beta\hat{q}\,\hat{p}\rangle = \varepsilon_{\alpha\beta\gamma\delta}\hat{p}^{\gamma}\hat{q}^{\delta}$ with the convention $\varepsilon_{0123} = +1$.

The covariant fermionic three-point vertex with the half-integer spin $s = n + 1/2$ is given by

$$[\Gamma_F] = \sum_{\tau=-n}^{n}\{[\hat{q}](\theta(\tau)f_{\tau+1}^{0}[P^{+}] + \theta(-\tau)f_{\tau-1}^{0}[P^{-}]) + f_{\tau}^{+}[W^{+}] + f_{\tau}^{-}[W^{-}]\}[S^{\hat{\tau}}]^{|\tau|}[S^{0}]^{n-|\tau|}, \tag{A21}$$

in terms of the fermionic f^0 and $f^{\pm}$ form factors, and "the covariant bosonic three-point vertex with the integer spin $s = n$ is given by

$$[\Gamma_B] = \sum_{\tau=-n}^{n}\{b_{\tau}^{0}[\hat{q}][S^{\hat{\tau}}] + \theta(|\tau|-1)(b_{\tau}^{+}[V_1^{\hat{\tau}}] + b_{\tau}^{-}[V_2^{\hat{\tau}}])\}[S^{\hat{\tau}}]^{|\tau|-1}[S^{0}]^{n-|\tau|}, \tag{A22}$$

in terms of the bosonic b^0 and $b^{\pm}$ form factors, where n is a non-negative integer and $\hat{\tau} = \tau/|\tau|$ satisfies $\hat{\tau} = +1$ for $\tau = 0$. Further, the step function $\theta(x) = 1$ is 1 or 0 for $x \geq 0$ or $x < 0$, respectively.

For two identical Majorana particles ($\chi_1 = \chi_2$) coupled to the U(1) gauge boson, the corresponding covariant three-point vertices Γ_F and Γ_B must satisfy the IP relations

$$C\Gamma_{F\beta,\alpha}^{\mu}(p,-q)C^{-1} = \Gamma_{F\alpha,\beta}^{\mu}(p,q) \quad \text{for fermions,} \tag{A23}$$

$$\Gamma_{B\beta,\alpha}^{\mu}(p,-q) = \Gamma_{B\alpha,\beta}^{\mu}(p,q) \quad \text{for bosons,} \tag{A24}$$

with the charge conjugation operator $C = i\gamma^2\gamma^0$ satisfying $CC^{\dagger} = 1$ and $C^{\dagger} = C^{T} = -C$. These IP relations lead to the following relations on the form factors:

$$f_{\tau\pm1}^{0} = 0, \qquad f_{\tau}^{+} = f_{\tau}^{-}, \tag{A25}$$

$$b_{\tau}^{0} = 0, \quad b_{\tau}^{+} = b_{\tau}^{-}, \tag{A26}$$

with $\tau = -n, \ldots, n$ for the non-negative integer n. As a result, we end up with the sum $W^{+} + W^{-}$ in the fermionic case and the sum $V_1^{\pm} + V_2^{\pm}$ in the bosonic case. Furthermore, imposing the U(1) gauge invariance condition on the summed expression, we can obtain the modified fermionic and bosonic vector operators[8]

$$A_{\mu} = \gamma_{\perp\mu}\gamma_5, \tag{A27}$$

$$V_{\mu}^{\pm} = \frac{1}{2}[\hat{p}_{\alpha}g_{\perp\alpha\mu} + \hat{p}_{\beta}g_{\perp\alpha\mu} \mp i\langle\alpha\beta\mu\hat{q}\rangle_{\perp}], \tag{A28}$$

with the orthogonal gamma matrix $\gamma_{\perp\mu} = g_{\perp\mu\nu}\gamma^{\nu}$ and the angle-bracket notation of the Levi-Civita tensor $\langle\alpha\beta\mu\hat{q}\rangle_{\perp} = g_{\perp\mu}{}^{\nu}\langle\alpha\beta\nu\hat{q}\rangle$ where the odd-parity operator $\langle\alpha\beta\mu\hat{q}\rangle_{\perp}$ is obtained through the effective replacement

$$\hat{p}_{\beta}\langle\alpha\mu\hat{p}\,\hat{q}\rangle - \hat{p}_{\alpha}\langle\beta\mu\hat{p}\,\hat{q}\rangle \overset{\text{eff}}{=} -\langle\alpha\beta\mu\hat{q}\rangle, \tag{A29}$$

which is guaranteed when the vertex operators are coupled to the wave tensors of two on-shell Majorana particles of spin s. For the detailed derivation, we refer to the works in Refs. [73,80–82,105]).

By gathering all the basic and derived operators, we can readily formulate the covariant representation of the effective hypercharge anapole vertices for a pair of identical Majorana particles with arbitrary spin

$$[\Gamma_B] = \sum_{\tau=-n}^{n}\theta(|\tau|-1)b_{\tau}[V^{\hat{\tau}}][S^{\hat{\tau}}]^{|\tau|-1}[S^{0}]^{n-|\tau|} \quad \text{for an integer spin } s = n, \tag{A30}$$

$$[\Gamma_F] = \sum_{\tau=-n}^{n} f_{\tau}[A][S^{\hat{\tau}}]^{|\tau|}[S^{0}]^{n-|\tau|} \quad \text{for a half-integer spin } s = n + 1/2, \tag{A31}$$

[8]The term $\hat{q}_{\mu}(\hat{q}\cdot\gamma)$ in $A_{\perp\mu}$ vanishes when coupled to the fermionic wave tensors due to their on-shell conditions.

which can be rendered equivalent to Eqs. (2.4) and (2.5) after a proper dimensional adjustment with the momentum-squareds, p^2 and q^2, and the cutoff scale Λ. The proper adjustment can easily be made by use of two effective identities

$$g_{\alpha\beta} = S^{+}_{\alpha\beta} + S^{-}_{\alpha\beta} - \frac{(p^2 - q^2)}{q^2} S^{0}_{\alpha\beta} \quad \text{and} \quad p_\alpha p_\beta = p^2 S^{0}_{\alpha\beta}, \tag{A32}$$

which are effectively valid due to their contractions with the wave tensors of two on-shell Majorana particles. As can be checked easily, the total number of independent terms is $2s$ both for the fermionic and bosonic cases as mentioned in Ref. [73].

APPENDIX B: CALCULATION STRATEGY OF THE DM RELIC ABUNDANCE

In this Appendix, we provide a detailed explanation of how to calculate the DM relic abundance. This abundance is determined by the thermal freeze-out processes illustrated in Fig. 2. In the absence of phase transitions, the entropy of the Universe in a comoving frame, $S \equiv sa^3 = (2\pi^2/45) g_s T^3 a^3$, with the degrees of freedom g_s contributing to the entropy density s is conserved throughout its evolution with the decreasing temperature T and, accordingly, the scale factor a. The freeze-out occurs during the radiation-dominated epoch, enabling us to write down the energy density $\rho = (\pi^2/30) g_\rho T^4$, with the degrees of freedom g_ρ, involved in the Hubble parameter $H = (1/a) da/dt = \sqrt{8\pi G\rho/3}$ with the gravitational constant G. In this case, the yield $Y(x)$ of DM particles, varying over $x = m_\chi/T$ (that is, over time and/or temperature), satisfies the so-called evolution equation,

$$\frac{dY}{dx} = -\frac{\lambda_{\rm ann}}{x^2} \frac{g_s}{\sqrt{g_\rho}} \left[1 + \frac{1}{3} \frac{d(\ln g_s)}{d(\ln T)}\right] (Y^2 - Y_{\rm eq}^2), \tag{B1}$$

where $\lambda_{\rm ann} = (\pi/45)^{1/2} M_{pl} m_\chi \langle \sigma v_{\rm M\o l} \rangle$ with the so-called Møller velocity $v_{\rm M\o l}$ of two annihilating DM particles [106] and $Y = n/s$ and $Y_{\rm eq} = n_{\rm eq}/s$ including the DM number density n and the thermal-equilibrium density $n_{\rm eq}$ in the comoving frame. Here, the yield $Y_{\rm eq}$ of the DM particles in thermal equilibrium can be written as

$$Y_{\rm eq}(x) = 0.1154 \frac{g_\chi}{g_s} x^2 K_2(x), \tag{B2}$$

with the DM spin degrees of freedom g_χ and the second-kind modified Bessel function K_2 of order 2. The simple asymptotic expression at large values of $x \gg 1$ is

$$Y_{\rm eq}(x) \approx 0.145 \frac{g_\chi}{g_s} x^{3/2} e^{-x}. \tag{B3}$$

In the present work, we calculate the thermally averaged cross section $\langle \sigma v_{\rm M\o l} \rangle$ by adopting its explicit form [106] as

$$\langle \sigma v_{\rm M\o l} \rangle = \frac{x}{8 m_\chi^5 K_2^2(x)} \int_{4m^2}^{\infty} ds \sqrt{s} (s - 4m_\chi^2) K_1(\sqrt{s}/T) \sigma(s), \tag{B4}$$

involving the annihilation cross sections in Eq. (3.1) or (3.2) with the second-kind modified Bessel function K_1 of order 1. This is because the conventional series expansions of the cross sections over the relative velocity between two annihilating DM particles do not converge when the annihilation energy $\sqrt{s}$ is close to the Z-boson mass due to the sharp Z-boson pole contribution [107]. The exponentially stiff suppression of the modified Bessel functions for large values of $x \gg 1$ renders the numerical calculation unreliable. Instead, we use its analytic asymptotic expression directly as

$$\langle \sigma v_{\rm M\o l} \rangle \sim \frac{x^{3/2}}{8 m_\chi^5} \sqrt{\frac{2m_\chi}{\pi}} \int_{4m_\chi^2}^{\infty} ds\, s^{1/4} (s - 4m_\chi^2) \times \exp\left[x\left(2 - \frac{\sqrt{s}}{m_\chi}\right)\right] \left(1 - \frac{15}{4x} + \frac{2m_\chi}{8x\sqrt{s}}\right) \sigma(s), \tag{B5}$$

for $x \gg 1$. The exclusion limits on the couplings satisfying the observed DM relic density $\Omega_\chi h^2 \approx 0.12$ [74] can be derived by integrating out Eq. (B1) from $x = 1$ to $x = 10^3$ with the initial condition $Y = Y_{\rm eq}$ at $x = 1$. Numerically, the function $\lambda_{\rm ann}$ dependent on the annihilation cross section varies stiffly with the DM mass m_χ in the GeV region, reducing the accuracy of the numerical calculation [108]. The numerical accuracy can be enhanced greatly by taking the integration after recasting the evolution equation as

$$\frac{dW}{dx} = -\frac{\lambda_{\rm ann}}{x^2} \frac{g_s}{\sqrt{g_\rho}} \left[1 + \frac{1}{3} \frac{d \ln g_s}{d \ln T}\right] [e^W - e^{(2W_{\rm eq} - W)}], \tag{B6}$$

with a more slowly varying logarithmic function $W = \ln Y$. The relic abundance calculations described so far are obtained semianalytically, and the results are consistent with the MICROMEGAS [109] calculations.

[1] M. Beltran, D. Hooper, E. W. Kolb, Z. A. C. Krusberg, and T. M. P. Tait, J. High Energy Phys. 09 (2010) 037.
[2] Q.-H. Cao, C.-R. Chen, C. S. Li, and H. Zhang, J. High Energy Phys. 08 (2011) 018.
[3] P. J. Fox, R. Harnik, J. Kopp, and Y. Tsai, Phys. Rev. D **85**, 056011 (2012).
[4] A. Belyaev, E. Bertuzzo, C. Caniu Barros, O. Eboli, G. Grilli Di Cortona, F. Iocco, and A. Pukhov, Phys. Rev. D **99**, 015006 (2019).
[5] S. L. Glashow, Nucl. Phys. **22**, 579 (1961).
[6] S. Weinberg, Phys. Rev. Lett. **19**, 1264 (1967).
[7] A. Salam, Conf. Proc. C **680519**, 367 (1968).
[8] H. Fritzsch, M. Gell-Mann, and H. Leutwyler, Phys. Lett. **47B**, 365 (1973).
[9] G. Aad *et al.* (ATLAS Collaboration), Phys. Lett. B **716**, 1 (2012).
[10] S. Chatrchyan *et al.* (CMS Collaboration), Phys. Lett. B **716**, 30 (2012).
[11] C. Arina, A. Cheek, K. Mimasu, and L. Pagani, Eur. Phys. J. C **81**, 223 (2021).
[12] M. Pospelov and T. ter Veldhuis, Phys. Lett. B **480**, 181 (2000).
[13] L. G. Cabral-Rosetti, M. Mondragón, and E. A. Reyes Pérez, J. Phys. Conf. Ser. **485**, 012019 (2014).
[14] L. G. Cabral-Rosetti, M. Mondragón, and E. Reyes-Pérez, Nucl. Phys. **B907**, 1 (2016).
[15] A. Ibarra, M. Reichard, and R. Nagai, J. High Energy Phys. 01 (2023) 086.
[16] H.-C. Cheng, J. L. Feng, and K. T. Matchev, Phys. Rev. Lett. **89**, 211301 (2002).
[17] G. Servant and T. M. P. Tait, Nucl. Phys. **B650**, 391 (2003).
[18] J. Hubisz and P. Meade, Phys. Rev. D **71**, 035016 (2005).
[19] A. Birkedal, A. Noble, M. Perelstein, and A. Spray, Phys. Rev. D **74**, 035002 (2006).
[20] T. Hambye, J. High Energy Phys. 01 (2009) 028.
[21] J. Hisano, K. Ishiwata, N. Nagata, and M. Yamanaka, Prog. Theor. Phys. **126**, 435 (2011).
[22] H. Davoudiasl and I. M. Lewis, Phys. Rev. D **89**, 055026 (2014).
[23] C. Gross, O. Lebedev, and Y. Mambrini, J. High Energy Phys. 08 (2015) 158.
[24] A. Karam and K. Tamvakis, Phys. Rev. D **92**, 075010 (2015).
[25] T. Flacke, D. W. Kang, K. Kong, G. Mohlabeng, and S. C. Park, J. High Energy Phys. 04 (2017) 041.
[26] S.-M. Choi, H. M. Lee, Y. Mambrini, and M. Pierre, J. High Energy Phys. 07 (2019) 049.
[27] F. Elahi and S. Khatibi, Phys. Rev. D **100**, 015019 (2019).
[28] T. Abe, M. Fujiwara, J. Hisano, and K. Matsushita, J. High Energy Phys. 07 (2020) 136.
[29] E. Nugaev and A. Shkerin, arXiv:2004.14354.
[30] F. Elahi and M. Mohammadi Najafabadi, Phys. Rev. D **102**, 035011 (2020).
[31] J. R. Ellis, J. S. Hagelin, D. V. Nanopoulos, K. A. Olive, and M. Srednicki, Nucl. Phys. **B238**, 453 (1984).
[32] M. Y. Khlopov and A. D. Linde, Phys. Lett. **138B**, 265 (1984).
[33] J. R. Ellis, J. E. Kim, and D. V. Nanopoulos, Phys. Lett. **145B**, 181 (1984).
[34] K. A. Olive, D. N. Schramm, and M. Srednicki, Nucl. Phys. **B255**, 495 (1985).
[35] Z.-H. Yu, J.-M. Zheng, X.-J. Bi, Z. Li, D.-X. Yao, and H.-H. Zhang, Nucl. Phys. **B860**, 115 (2012).
[36] R. Ding and Y. Liao, J. High Energy Phys. 04 (2012) 054.
[37] K. G. Savvidy and J. D. Vergados, Phys. Rev. D **87**, 075013 (2013).
[38] R. Ding, Y. Liao, J.-Y. Liu, and K. Wang, J. Cosmol. Astropart. Phys. 05 (2013) 028.
[39] M. O. Khojali, A. Goyal, M. Kumar, and A. S. Cornell, Eur. Phys. J. C **77**, 25 (2017).
[40] M. O. Khojali, A. Goyal, M. Kumar, and A. S. Cornell, Eur. Phys. J. C **78**, 920 (2018).
[41] C.-F. Chang, X.-G. He, and J. Tandean, Phys. Rev. D **96**, 075026 (2017).
[42] M. A. G. Garcia, Y. Mambrini, K. A. Olive, and S. Verner, Phys. Rev. D **102**, 083533 (2020).
[43] K.-y. Wu and A. Lee, arXiv:2203.13720.
[44] A. Goyal, M. O. Khojali, M. Kumar, and A. S. Cornell, Eur. Phys. J. C **82**, 1002 (2022).
[45] K. Kaneta, W. Ke, Y. Mambrini, K. A. Olive, and S. Verner, Phys. Rev. D **108**, 115027 (2023).
[46] N. Arkani-Hamed, S. Dimopoulos, and G. R. Dvali, Phys. Rev. D **59**, 086004 (1999).
[47] J. L. Feng, A. Rajaraman, and F. Takayama, Phys. Rev. D **68**, 085018 (2003).
[48] S. L. Dubovsky, P. G. Tinyakov, and I. I. Tkachev, Phys. Rev. Lett. **94**, 181102 (2005).
[49] M. Pshirkov, A. Tuntsov, and K. A. Postnov, Phys. Rev. Lett. **101**, 261101 (2008).
[50] K. Aoki and S. Mukohyama, Phys. Rev. D **94**, 024001 (2016).
[51] E. Babichev, L. Marzola, M. Raidal, A. Schmidt-May, F. Urban, H. Veermäe, and M. von Strauss, Phys. Rev. D **94**, 084055 (2016).
[52] E. Babichev, L. Marzola, M. Raidal, A. Schmidt-May, F. Urban, H. Veermäe, and M. von Strauss, J. Cosmol. Astropart. Phys. 09 (2016) 016.
[53] K. Aoki and K.-i. Maeda, Phys. Rev. D **97**, 044002 (2018).
[54] K. Aoki and S. Mukohyama, Phys. Rev. D **96**, 104039 (2017).
[55] X. Chu and C. Garcia-Cely, Phys. Rev. D **96**, 103519 (2017).
[56] N. L. González Albornoz, A. Schmidt-May, and M. von Strauss, J. Cosmol. Astropart. Phys. 01 (2018) 014.
[57] M. Garny, A. Palessandro, M. Sandora, and M. S. Sloth, J. Cosmol. Astropart. Phys. 02 (2018) 027.
[58] K. Aoki, K.-i. Maeda, Y. Misonoh, and H. Okawa, Phys. Rev. D **97**, 044005 (2018).
[59] H. Cai, G. Cacciapaglia, and S. J. Lee, Phys. Rev. Lett. **128**, 081806 (2022).
[60] Y. Manita, K. Aoki, T. Fujita, and S. Mukohyama, Phys. Rev. D **107**, 104007 (2023).
[61] M. A. Gorji, J. Cosmol. Astropart. Phys. 11 (2023) 081.
[62] C. M. Ho and R. J. Scherrer, Phys. Lett. B **722**, 341 (2013).
[63] C. M. Ho and R. J. Scherrer, Phys. Rev. D **87**, 065016 (2013).
[64] Y. Gao, C. M. Ho, and R. J. Scherrer, Phys. Rev. D **89**, 045006 (2014).

[65] B. Geytenbeek, S. Rao, P. Scott, A. Serenelli, A. C. Vincent, M. White, and A. G. Williams, J. Cosmol. Astropart. Phys. 03 (2017) 029.
[66] D. C. Latimer, Phys. Rev. D **95**, 095023 (2017).
[67] A. Alves, A. C. O. Santos, and K. Sinha, Phys. Rev. D **97**, 055023 (2018).
[68] S. Kang, S. Scopel, G. Tomar, J.-H. Yoon, and P. Gondolo, J. Cosmol. Astropart. Phys. 11 (2018) 040.
[69] A. Flórez, A. Gurrola, W. Johns, J. Maruri, P. Sheldon, K. Sinha, and S. R. Starko, Phys. Rev. D **100**, 016017 (2019).
[70] D. Bose, D. Chowdhury, P. Mondal, and T. S. Ray, arXiv:2312.05131.
[71] J. Hisano, A. Ibarra, and R. Nagai, J. Cosmol. Astropart. Phys. 10 (2020) 015.
[72] X. Chu, J. Hisano, A. Ibarra, J.-L. Kuo, and J. Pradler, Phys. Rev. D **108**, 015029 (2023).
[73] F. Boudjema and C. Hamzaoui, Phys. Rev. D **43**, 3748 (1991).
[74] N. Aghanim *et al.* (Planck Collaboration), Astron. Astrophys. **641**, A6 (2020); **652**, C4(E) (2021).
[75] E. Aprile *et al.* (XENON Collaboration), Phys. Rev. Lett. **131**, 041003 (2023).
[76] V. Shiltsev and F. Zimmermann, Rev. Mod. Phys. **93**, 015006 (2021).
[77] G. Aad *et al.* (ATLAS Collaboration), Phys. Rev. D **103**, 112006 (2021).
[78] A. Tumasyan *et al.* (CMS Collaboration), J. High Energy Phys. 11 (2021) 153.
[79] R. Assmann, P. McIntosh, A. Fabris, G. Bisoffi, I. Andrian, and G. Vinicola, *Proceedings of the 14th International Particle Accelerator Conference (IPAC'2023)* (JACoW, Geneva, Switzerland, 2023), TUYG1, https://dx.doi.org/10.18429/JACoW-IPAC2023.
[80] S. Y. Choi and J. H. Jeong, Phys. Rev. D **103**, 096013 (2021).
[81] S. Y. Choi and J. H. Jeong, Phys. Rev. D **104**, 055046 (2021).
[82] S. Y. Choi and J. H. Jeong, Phys. Rev. D **105**, 016016 (2022).
[83] A. Denner, H. Eck, O. Hahn, and J. Kublbeck, Phys. Lett. B **291**, 278 (1992).
[84] A. Denner, H. Eck, O. Hahn, and J. Kublbeck, Nucl. Phys. **B387**, 467 (1992).
[85] R. E. Behrends and C. Fronsdal, Phys. Rev. **106**, 345 (1957).
[86] P. R. Auvil and J. J. Brehm, Phys. Rev. **145**, 1152 (1966).
[87] P. J. Caudrey, I. J. Ketley, and R. C. King, Nucl. Phys. **B6**, 671 (1968).
[88] M. D. Scadron, Phys. Rev. **165**, 1640 (1968).
[89] S. U. Chung, Phys. Rev. D **57**, 431 (1998).
[90] S.-Z. Huang, T.-N. Ruan, N. Wu, and Z.-P. Zheng, Eur. Phys. J. C **26**, 609 (2003).
[91] A. Chakraborty, S. Kuttimalai, S. H. Lim, M. M. Nojiri, and R. Ruiz, Eur. Phys. J. C **78**, 679 (2018).
[92] G. Frattari, Nuovo Cimento C **43**, 32 (2020).
[93] A. Abada *et al.* (FCC Collaboration), Eur. Phys. J. Special Topics **228**, 755 (2019).
[94] M. Benedikt, A. Blondel, P. Janot, M. Mangano, and F. Zimmermann, Nat. Phys. **16**, 402 (2020).
[95] K. Agashe, Y. Cui, L. Necib, and J. Thaler, J. Cosmol. Astropart. Phys. 10 (2014) 062.
[96] D. Kim, J.-C. Park, and S. Shin, Phys. Rev. Lett. **119**, 161801 (2017).
[97] G. F. Giudice, D. Kim, J.-C. Park, and S. Shin, Phys. Lett. B **780**, 543 (2018).
[98] H. Alhazmi, D. Kim, K. Kong, G. Mohlabeng, J.-C. Park, and S. Shin, J. High Energy Phys. 05 (2021) 055.
[99] R. H. Helm, Phys. Rev. **104**, 1466 (1956).
[100] J. D. Lewin and P. F. Smith, Astropart. Phys. **6**, 87 (1996).
[101] S. Chang, N. Weiner, and I. Yavin, Phys. Rev. D **82**, 125011 (2010).
[102] J. Aalbers *et al.*, J. Phys. G **50**, 013001 (2023).
[103] M. Jacob and G. C. Wick, Ann. Phys. (N.Y.) **7**, 404 (1959).
[104] M. Rose, *Elementary Theory of Angular Momentum*, Dover Books on Physics Series (Dover, Incorporated, 2013), ISBN: 9780486788791.
[105] K. Hagiwara, R. D. Peccei, D. Zeppenfeld, and K. Hikasa, Nucl. Phys. **B282**, 253 (1987).
[106] P. Gondolo and G. Gelmini, Nucl. Phys. **B360**, 145 (1991).
[107] K. Griest and D. Seckel, Phys. Rev. D **43**, 3191 (1991).
[108] G. Steigman, B. Dasgupta, and J. F. Beacom, Phys. Rev. D **86**, 023506 (2012).
[109] G. Bélanger, F. Boudjema, A. Goudelis, A. Pukhov, and B. Zaldivar, Comput. Phys. Commun. **231**, 173 (2018).